

**Rocking and rolling down an incline: the dynamics
of nested cylinders on a ramp**

by

David Paul Vener

B.S. Applied Mathematics, Georgia Institute of Technology, 2001

B.S. Physics, Georgia Institute of Technology, 2001

Submitted to the Department of Mathematics

in partial fulfillment of the requirements for the degree of

DOCTOR OF PHILOSOPHY

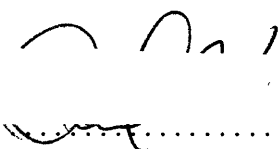
at the

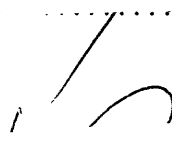
MASSACHUSETTS INSTITUTE OF TECHNOLOGY

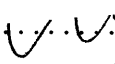
June 2006

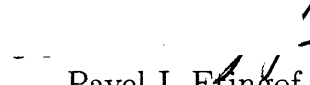
©David Paul Vener, 2006. All Rights Reserved.

The author hereby grants to MIT permission to reproduce and
distribute publicly paper and electronic copies of this thesis document
in whole or in part.

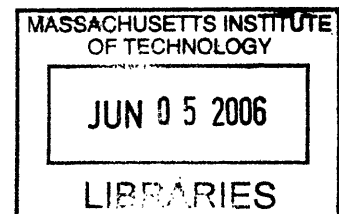
Author 
Department of Mathematics
May 12, 2006

Certified by 
John W. M. Bush
Associate Professor
Thesis Supervisor

Accepted by 
Rodolfo Ruben Rosales
Chairman, Applied Mathematics Committee

Accepted by 
Pavel I. Etingof
Chairman, Department Committee on Graduate Students

ARCHIVES



Rocking and rolling down an incline: the dynamics of nested cylinders on a ramp

by

David Paul Vener

Submitted to the Department of Mathematics
on May 12, 2006, in partial fulfillment of the
requirements for the degree of
DOCTOR OF PHILOSOPHY

Abstract

In this thesis, I report the results of a combined experimental and theoretical investigation of a journal bearing, specifically, a cylinder suspended in a viscous fluid housed within a cylindrical shell, rolling down an incline under the influence of gravity. Particular attention is given to rationalizing the distinct modes of motion observed. We performed a series of experiments in which the inner cylinder density and the fluid viscosity were varied. Three distinct types of behavior were observed. First, in what we shall call the “rocking” mode, after an initial settling period, the shell rocks back and forth without moving down the ramp. Second, we observed “slow, quasi-steady rolling”; this mode is characterized by the system proceeding down the hill at essentially a constant velocity. Finally, the cylinders roll down the incline with constant acceleration; we shall call this mode “unbounded acceleration.” An accompanying theoretical model is developed and enables us to rationalize the rocking and accelerating modes. In the rocking solutions, potential and kinetic energy are dissipated in the fluid as the inner cylinder approaches the bottom of the outer cylinder. In the accelerating solutions, the whole system moves as a solid body so that no dissipation occurs and potential energy is continually converted into kinetic energy. In order to understand the quasi-steady motion, we analyze the motion of a similar system: a metal cylinder is placed inside a larger plastic cylinder filled with fluid and attached to a motor which fixes the larger cylinder’s rotation rate. Our observations of this system, specifically, the differences between experiments and theory lead us to consider the effect of internal friction due to surface roughness. The resulting model’s predictions are well supported by our observations. Finally, to rationalize the slow, quasi-steady rolling motion of the system, we incorporate surface roughness and cavitation into the theoretical model. These effects provide a restoring force on the inner cylinder; however, we find that surface roughness is the dominant effect.

Thesis Supervisor: John W. M. Bush
Title: Associate Professor

Acknowledgments

I'd like to take this opportunity to thank some of the many people whose academic and personal efforts have made writing this thesis possible.

On the academic side, I'd first like to thank Neil Balmforth whose ideas were my main guide through the problem. Bill Young was invaluable in getting past several mathematical hurdles that appeared along the way. My advisor, John Bush, first conceived of the problem, and his guidance made this thesis both more readable and more understandable. Finally, the other members of my thesis committee, Ruben Rosales, Peko Hosoi, and Darren Crowdy, also provided great suggestions which I have done my best to incorporate into this final version.

Since a doctoral thesis is such a large project, one's personal life invariably becomes involved in its completion. Without Ellen Weinstein's support I could not have gotten through the last year of this process. Nicole Simi also provided a great deal of valuable guidance over the past three years. I'd also like to mention Bobak Ferdowsi, Kim Clarke, Heidi Davidz, and Christine Taylor who made Cambridge a fun place for several years. Finally, I'd like to thank Wes Gifford, Jaehyuk Choi, Eugene Weinstein, and Parag Vaidya for making my living space livable.

Contents

1	Introduction	19
2	Initial observations	23
2.1	The snail cylinder	23
2.1.1	Laboratory set-up	23
2.1.2	Observations	25
2.2	Experiments with the fixed outer cylinder	26
2.2.1	Laboratory set-up	26
2.2.2	Observations	27
2.3	Bubbles	29
3	Formulation of the rolling problem	31
3.1	Geometry	31
3.2	Dynamical equations for the cylinder centers	33
3.2.1	Motion of the inner center relative to the outer center: the ϵ equation	35
3.2.2	Rotational equations of motion	36
3.3	Hydrodynamic forces and torques	36
3.3.1	Lubrication analysis	37
3.3.2	The rotational flow, $\mathbf{u}^R(z, \theta)$	38
3.3.3	The squeeze flow, $\mathbf{u}^S(z, \theta)$	39
3.3.4	Calculating forces and torques	39
3.4	Closing the equations of motion	41

3.4.1	Understanding (3.44) in terms of total angular momentum . . .	41
3.5	A steady solution	43
3.6	A quasi-steady solution	44
3.7	Energetics	45
4	A reduced lubrication model	49
4.1	Reduction of the dynamics	49
4.2	An useful recasting of the reduced system	51
4.3	The sedimenting solution with $s = 0$	51
4.4	Solutions with $s \neq 0$	52
4.4.1	The Sommerfeld equilibrium	52
4.4.2	Other solutions	53
4.4.3	Numerical solutions	54
4.5	Shortcomings of the model	56
5	Theoretical formulation of the stationary mixer problem	59
5.1	Geometry	59
5.2	Dynamic equations for the inner cylinder center	61
6	Dimensionless formulation of the fixed outer cylinder system	65
6.1	Determining the dimensionless system	65
6.2	The journal bearing	67
6.3	The fixed outer cylinder	69
6.3.1	Adding a sliding contact	73
6.4	Summary	76
7	Experiments	77
7.1	Comparison of simulation and experiment with the fixed outer cylinder	77
7.2	Additional experiments with the snail cylinders	82
8	Rough contact and cavitation in the rolling system	87
8.1	Cavitation	87

8.2 Rough contact	91
9 Conclusions	97
A Dimensionless groups and physical quantities	101
B The Calculations of Finn and Cox[8]	103
B.1 Rotlets and Stokeslets	103
B.2 Forces and torques from the stream function	106

List of Figures

2-1	Photographs showing various views of the snail cylinder. In order of appearance, the views are (a) angled from the front, (b) angled from behind, (c) face on from the front, and (d) edge on. Note that several small bubbles are trapped inside and have risen to the top of the fluid, and that the inner cylinder lies along the base of the outer cylinder.	24
2-2	Distance traveled along the runway for an aluminum inner cylinder with a slope of 5° . Four experiments are shown: a first pair of repeated runs with $\nu = 2 \times 10^{-4}$ (dots and solid lines), and a second pair with $\nu = 3.5 \times 10^{-4}$ (circles and dashed lines). Also shown is the function, $(gt^2 \sin \alpha)/3$, expected for a solid cylinder (dotted lines).	25
2-3	Distance traveled along the runway for a steel inner cylinder with various slopes. Panel (a) shows a long run at 2.4° ; the inset shows a magnification of the path. Panel (b) shows four different slopes, as marked. The dotted lines show the best-fit linear fits calculated for all the experiments.	26
2-4	The experimental apparatus	27
2-5	The various observed modes. Rotation speed increases from left to right.	28
3-1	The geometry. The point B is the center of the outer, hollow cylinder (radius b) and A is the center of the inner solid cylinder (radius a). The displacement vector from A to B is $\epsilon(t)$. The ‘line of centers’ is BAO . The origin of the gap coordinate system, $(z, \theta) = (0, 0)$ is the point O . If the center of mass of the apparatus lies on vertical line CD then the torque on the right hand side of (3.44) vanishes.	32

3-2	The instantaneous speeds associated with points on the surface of the two cylinders.	37
4-1	Sample rocking solution with $\Upsilon = 1$, $m_b = 0$ ($M = m_a$) and $s = 1/4$. The panels show (a) the locus of the center of the inner cylinder on the polar (κ, β) plane (with $\beta = 0$ pointing vertically downwards), (b) $\kappa(t)$, (c) $\beta(t)$ and $X_b(t)$ (blue and red, respectively), and (d) $\Omega_a(t)$ and $\Omega_b(t)$ (blue and red, respectively). The initial position of the inner cylinder is shown, and $\Omega_a(0) = \Omega_b(0) = 0$. The star in the polar plot marks the limiting sedimentation solution.	55
4-2	Sample rocking solution with $\Upsilon = 1$, $m_b = 0$ ($M = m_a$) and $s = .9$. The layout of the figure is largely as in figure 4-1. The cylinders are initially at rest.	55
4-3	Instability of the Sommerfeld solution for $\Upsilon = 1$, $m_b = 0$ and $s = 1/4$. The layout of the figure is largely as in figure 4-1. Initial conditions are chosen very close to the Sommerfeld fixed point (indicated by the circle).	56
5-1	The geometry. The point B is the center of the outer, hollow cylinder (radius b) and A is the center of the inner solid cylinder (radius a). The ‘line of centers’ is BAO	60
6-1	The relation between $\hat{\Omega}_b$, Ω_{a*} and κ_* for several values of $\hat{\delta} = (b - a)/a$ (as labeled).	70
6-2	Stability boundaries of the equilibrium point on the $(\hat{\delta}, \kappa_*)$ -plane for several values of γ (as indicated). Note that γ is defined in (6.5), κ_* is defined by (6.27), and $\hat{\delta} = (b - a)/a$	70

6-3	Phase portraits and time series for $\hat{\delta} = 0.5$, $\kappa_* = 0.5$ and $\gamma = 0.1$. The phase portrait shows the locus of the center of the inner cylinder on the (X_i, Z_i) -plane. The outer circle shows the limiting curve on which the inner cylinder touches the outer one, and the star shows the equilibrium point, $(\hat{\delta}\kappa_*, 0)$. The time series of $\kappa(t)$ also shows κ_* , and the horizontal lines in the plot of $\hat{\Omega}_a(t)$ show $\hat{\Omega}_b$ and $\hat{\Omega}_{a*}$	71
6-4	Phase portraits and time series for $\hat{\delta} = 0.3$, $\kappa_* = 0.4$ and $\gamma = 0.01$. The phase portrait shows the locus of the center of the inner cylinder on the (X_i, Z_i) -plane. The outer circle shows the limiting curve on which the inner cylinder touches the outer one, and the star shows the equilibrium point, $(\hat{\delta}\kappa_*, 0)$. Two solutions are shown; one converges to the stable equilibrium, the other diverges towards the outer cylinder. The time series of $\kappa(t)$ also shows κ_* , and the horizontal lines in the plot of $\hat{\Omega}_a(t)$ show $\hat{\Omega}_b$ and $\hat{\Omega}_{a*}$	72
6-5	Phase portraits and time series for $\hat{\delta} = 0.176$, $\kappa_* = 0.93$ and $\gamma = 0.02$. The phase portrait shows the locus of the center of the inner cylinder on the (X_i, Z_i) -plane. The outer circle shows the limiting curve on which the inner cylinder touches the outer one, and the star shows the equilibrium point, $(\hat{\delta}\kappa_*, 0)$. Two solutions are shown, each converging to a stable limit cycle. The time series of $\kappa(t)$ also shows κ_* , and the horizontal lines in the plot of $\hat{\Omega}_a(t)$ show $\hat{\Omega}_b$ and $\hat{\Omega}_{a*}$	73
6-6	Sliding inner cylinder: Phase portraits of the locus of the center of the inner for $\hat{\delta} = 2$, $\gamma = 0.1$ and several values of κ_* (top row: 0.999, 0.996, 0.993, 0.99, middle row: 0.984, 0.983, 0.982, 0.981, bottom row: 0.98 and 0.978), which correspond to a sequence of increasing rotation rates of the outer cylinder.	75
7-1	Experimental observations collected with decreasing Re . $Re \equiv \Omega_b b^2 / \nu$ is plotted against $Fr = \Omega_b^2 b / g'$, with $g' = g(\rho_a - \rho_f) / \rho_f$. Modes correspond to those defined in figure 2-5.	79

7-2	Experimental observations collected with increasing Re . $Re \equiv \Omega_b b^2 / \nu$ is plotted against $Fr = \Omega_b^2 b / g'$, with $g' = g(\rho_a - \rho_f) / \rho_f$	80
7-3	Numerically simulated results with $\kappa_m = .98$ are plotted with the observed behavior from figure 7-1. $Re \equiv \Omega_b b^2 / \nu$ is plotted against $Fr = \Omega_b^2 b / g'$, with $g' = g(\rho_a - \rho_f) / \rho_f$. The numerical points are the plus signs.	81
7-4	The average speeds fitted to the experiments. Panel (a) shows the raw data, plotted against slope, with the different symbols corresponding to different viscosities (as labeled in centipoise) and inner cylinders. In panel (b) we scale the speeds by the factor, V_* , in (7.7), and add rough estimates of the error bars. The two lines show theoretical predictions assuming $\varepsilon = 0.1$ and 0.2 in (8.30). The data shown by green circles indicate measurements taken for 500 centiStoke oil in which a large number of small bubbles are entrained in the fluid and migrate into the narrowest part of the gap between the cylinders to form a line of cavitation.	83
7-5	The average speeds of the two cylinders, $\langle V_a \rangle = a \langle \Omega_a \rangle$ (stars) and $\langle V_b \rangle = b \langle \Omega_b \rangle$ (dots), against slope for the steel inner cylinder and (a) 500 centiStoke and (b) 60 centiStoke oil.	84
7-6	Panel (a) shows the average speeds of the outer cylinder scaled by V_* plotted against slope for the steel inner cylinder and 500 centiStoke silicone oil. The stars indicate the speeds with the usual, smooth cylinder. The circles show the speeds when the inner cylinder is covered by rough sandpaper with varying scales of roughness, as indicated. In panel (b), a further scaling of ε is used to collapse the data. The values used are calculated using the roughness scales listed in table 7.1.	85
8-1	In panel (a), normalized pressure, $p(\theta)$, is plotted for $\kappa_m = 0.9$ with $(6a^2 \rho \nu / \delta^2) (\Omega_a + \Omega_b - \dot{\beta}) \equiv 1$. In panel (b), r (defined in (8.13)) is plotted versus κ_m , the minimum gap size.	88

8-2	Sample rocking solution for $\Upsilon = 1$, $m_b = 0$ ($M = m_a$) and $s = 1/4$, with κ limited to the range $(0, \kappa_m = 0.98)$, and $\psi = 0.05$. The layout of panels (a)-(d) is as for figure 4-1, except that the unlimited sedimenting solution is also shown by the dotted lines.	94
8-3	Sample solution for $\Upsilon = 1$, $m_b = 0$ ($M = m_a$) and $s = 1/4$, with $\kappa_m = 0.98$ and four values of ψ (0.5, 0.05, 0.1 and 0; the curves are offset of clarity). The vertical dashed line shows the moment of contact.	94
8-4	Scaled, steady rotation rates, $\Omega_a/(3\zeta_m)$ and $\Omega_b/(3\zeta_m)$, for $\phi = 0.15$	95

List of Tables

2.1	Physical data. The viscosity of the oil (Dow Corning 200 fluid) was approximately 5×10^{-5} , 2×10^{-4} and 3.5×10^{-4} m ² /sec. The perspex outer cylinder was 1.5mm thick. The runway was inclined by the angles: 1.4°, 2.4°, 3.3°, 4.2°, 5° and 5.6°.	24
2.2	Physical parameters for the model. The fluid is assumed to largely fill the gap between the two cylinders and have negligible mass at the ends (we estimate there to be about 4 g of the total 24 g actually at the ends).	24
7.1	Roughness scales for the various grades of sandpaper (as given by the “grit” value listed). The “measured” value indicates the number used to collapse the data in figure 7-6; the “expected” value is the number quoted by the American CAMI standard and refers to average particle size.	85
A.1	Various dimensionless groups used in the thesis	102
A.2	Various physical quantities and their meanings	102

Chapter 1

Introduction

We consider two problems related to the dynamics of a hollow cylindrical shell filled with fluid and another rigid cylinder and placed on an incline. This work is also being reported in two papers in preparation[4, 3]. This study was inspired by the commercially available “snail ball,”¹ a smooth gold ball that feels solid to the touch and when shaken, but rolls very slowly down an incline. The slow movement is a consequence of the ball containing a heavy weight and a viscous fluid. The associated internal dissipation greatly impedes the ball’s progress.

First, an experimental and theoretical investigation of an analogous cylindrical system where a heavy cylinder is placed inside a fluid filled outer cylinder is considered. This “snail cylinder” exhibits several different behaviors when placed on an incline: rocking back and forth, slow quasi-steady rolling, and unbounded acceleration. In the rocking modes, the outer cylinder is observed to oscillate with decreasing amplitude around a pivot point; the system makes no net progress down the incline. When the system makes slow progress down the incline at low speed, we call this quasi-steady rolling. In this mode, we observe some jerking, but the average velocity may be taken as constant. Finally, we observed a mode characterized by almost constant acceleration as the system rolls down the incline; we call this mode unbounded acceleration. In order to rationalize our observations, we develop a theoretical model valid in the limit that the gap space between the cylinders is very small.

¹The snail ball can be purchased at http://www.grand-illusions.com/toyshop/snail_ball

In order to test the range of validity of our model, we then consider a similar system, in which the space between the cylinders may be arbitrary in size, but the outer cylinder is held at a constant angular velocity. A series of experiments were performed. We then develop a hierarchy of reduced theoretical models of increasing complexity in order to examine the dynamics in several limits. We briefly look at the classical journal bearing limit to verify that the model agrees with previous results. Next we allow the inner cylinder to move and rotate freely and investigate the resulting dynamics. In order to account for a marked discrepancy between experiments and theory, we then add surface roughness effects to the model and compare its predictions to our laboratory observations. We conclude this thesis by considering the influence of surface roughness and cavitation on the motion of the original snail cylinder system. These effects ultimately allow us to explain the snail cylinder's curious quasi-steady slow rolling motion.

Reynolds appears to be the first to look at the dynamics of nested cylinders; he considered the special case where the radii of the cylinders only differs by a small amount so that the gap between them is small everywhere [16]. This corresponds to the lubrication approximation for the journal bearing, a problem that has subsequently been well studied, owing to its many direct applications to large industrial machinery, such as steam turbines and large motors. In these applications, the bearing (i.e. the outer cylinder) serves as a rotor support, providing a low-friction environment to protect and guide a rotating shaft. Due in part to its usefulness, the journal bearing has been treated exhaustively in the engineering literature. When designing large, expensive equipment, an engineer wants to understand the flow within the bearing to prevent instabilities that could lead to chaotic motion, unpredictable results, and, possibly, damage to the equipment. Pinkus and Sternlicht discuss various aspects of the problem in their textbook on hydrodynamic lubrication. These include dynamically loaded bearings and hydrodynamic instabilities within the bearing. They also discuss fluid inertia and turbulence effects on the the fluid flow [13]. More recent research has concentrated on the nonlinear interactions between the fluid and the rotor. In particular, Brindley, Savage and Taylor perform a numerical study of an

incomplete bearing, in which the gap is not entirely filled with lubricating fluid [6].

The journal bearing is just one example of a larger class of fluid dynamics problems called lubrication theory. One may easily notice that two solids slide over each other much more easily when they are separated by a thin layer of fluid. Because the fluid layer is so small, a large pressure may develop holding the surfaces apart which reduces friction between them [5]. Mathematically, the lubrication approximation implies that the nonlinear inertial forces within the fluid are dominated by the linear pressure and viscous forces. General lubrication is also very prominent in the engineering literature. For example, Pinkus and Sternlicht apply the approximation to thrust bearings, squeeze films, and dynamically loaded bearing. In addition, they consider modifications to the theory to account for several types of fluid instability, the use of non-Newtonian fluids, and several other applications [13].

Zhukowski, Jeffrey, Dufing, Reissner, and others have all calculated the load necessary to hold the location of both cylinders fixed while maintaining their rotational speeds for any sized gap between the cylinders [22, 10, 7, 15]. Then Ballal and Rivlin make the same calculation, adding inertial effects [2]. Each of these authors does this calculation for arbitrary differences in the radii by using a specific curvilinear coordinate reference frame to solve the biharmonic equation for the stream function in the case that both cylinders are held stationary. Wannier, however, discovered a more general complex variable technique to solve nested cylinder problems [20]. The complex methods of Wannier have since been extended to describe the case where the center of mass of the inner cylinder is also allowed to move. Finn and Cox adapted these methods and the work of Stevenson to determine the forces on the inner and outer cylinders in terms of the geometric parameters of the system by using an application of the images of point rotlets and stokeslets in the outer cylinder [8, 19]. These forces will be adapted in our study of the nested cylinders holding the outer cylinder's rotation rate constant in section 5.2. Recently, Yue also studied this system, concentrating on boundary integral techniques to compute trajectories of the inner cylinder [21].

Much work also has been done on problems related to objects moving near a

solid wall in a Stokes flow. Goldman, Cox, and Brenner [9] discuss the motion of a sphere moving vertically next to a plane wall in a viscous fluid by solving the Stokes equations exactly in this geometry. Close to the wall, surface effects such as roughness or cavitation can affect the motion of the moving object. Cavitation occurs when the pressure in the fluid gap falls below the vapor pressure in the fluid, at which small bubbles precipitate out of solution. Goldman, et al., consider that cavitation could account for the failure of their theory to match the observed motion of a neutrally buoyant sphere in Stokes flow adjacent to a vertical wall [9]. Several other authors have done experimental studies of the cavitation of slowly moving spheres [12, 14]. Smart, Beimfohr, and Leighton discuss the effect of surface roughness on the motion of the sphere rolling down a flat incline [18]. Tom Mullin and his group have performed experiments with both spheres and cylinders moving near the wall of a rotating outer cylinder [11]. They also observe cavitation bubbles in their experiments and consider the effect it has on the inner body. Seddon and Mullin perform experiments using cylinders and propose that cavitation may reverse the direction that the inner cylinder rotates [17]. Ashmore, del Pino, and Mullin develop an analytical theory of cavitation to describe their observations of spheres near the wall of a rotating cylinder [1]. Their work was adapted in our cavitation analysis in section 8.1.

We first report the results of several initial experiments performed with the snail cylinders and the simpler system in which the outer cylinder is rotated at a prescribed constant rate. We proceed in chapters 3 and 4 by modeling the snail cylinders numerically but find that the model as formulated does not fully match our observations. Chapters 5 and 6 detail our model of the simpler system. We find that to rationalize the observations in chapter 2, we must incorporate surface roughness effects into our model. In chapter 7 we perform additional experiments with the fixed outer cylinder and compare the results with the theory from chapter 6. We then report the results of a more detailed set of experiments with several different roughness scales using the snail cylinders. Finally, in chapter 8, we add surface roughness to the snail ball theory constructed in chapter 4 and find that this effect dominates that of cavitation.

Chapter 2

Initial observations

In this section we present our initial observations of the snail cylinders using two different weights and several fluids of differing viscosities. Special attention is paid to the low-slope regime where a quasi-steady rolling mode appears that does not accelerate indefinitely. To better understand this mode, we also performed experiments on a simplified system in which the outer cylinder's rotation rate is prescribed by a motor.

2.1 The snail cylinder

2.1.1 Laboratory set-up

A photograph of the apparatus used in our experiment is shown in figure 2-1. A perspex tube filled with silicone oil and containing a steel or aluminum inner cylinder rolls without sliding down an inclined runway. The ends of the tube are stoppered by black rubber corks. Metal nails are inserted through the middle of each cork so that a sharp point intrudes slightly into the fluid and prevents the inner cylinder from impinging on the corks. Physical data for the apparatus is given in table 2.1; the corresponding physical parameters are listed in table 2.2.

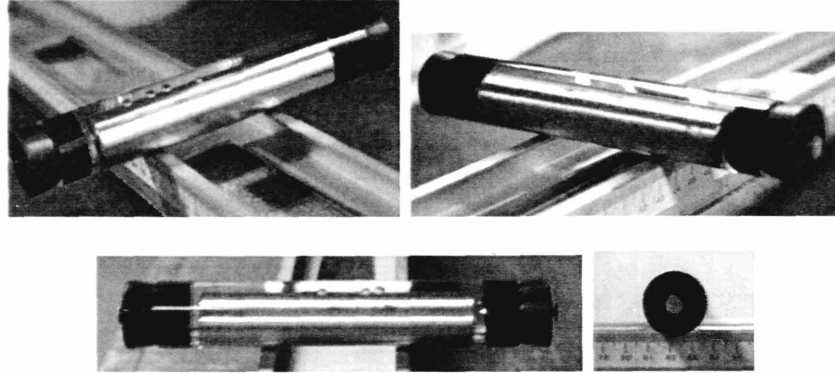


Figure 2-1: Photographs showing various views of the snail cylinder. In order of appearance, the views are (a) angled from the front, (b) angled from behind, (c) face on from the front, and (d) edge on. Note that several small bubbles are trapped inside and have risen to the top of the fluid, and that the inner cylinder lies along the base of the outer cylinder.

	Density	Radius	Mass	Length
Steel inner cylinder	7.85 g/cm ³	0.8 cm	155 g	10.35 cm
Aluminum inner cylinder	2.7 g/cm ³	0.8 cm	54 g	10.35 cm
Outer cylinder		1.125 cm	46 g	13.7 cm
Silicone oil	1 g/cm ³		24 g	

Table 2.1: Physical data. The viscosity of the oil (Dow Corning 200 fluid) was approximately 5×10^{-5} , 2×10^{-4} and 3.5×10^{-4} m²/sec. The perspex outer cylinder was 1.5mm thick. The runway was inclined by the angles: 1.4°, 2.4°, 3.3°, 4.2°, 5° and 5.6°.

a	δ	L	m_b
0.8 cm	0.325 cm	10.35 cm	46 g

	M	m_a	m'_a	m''_a
Steel	225 g	155 g	131 g	65 g
Aluminum	124 g	54g	30 g	65 g

Table 2.2: Physical parameters for the model. The fluid is assumed to largely fill the gap between the two cylinders and have negligible mass at the ends (we estimate there to be about 4 g of the total 24 g actually at the ends).

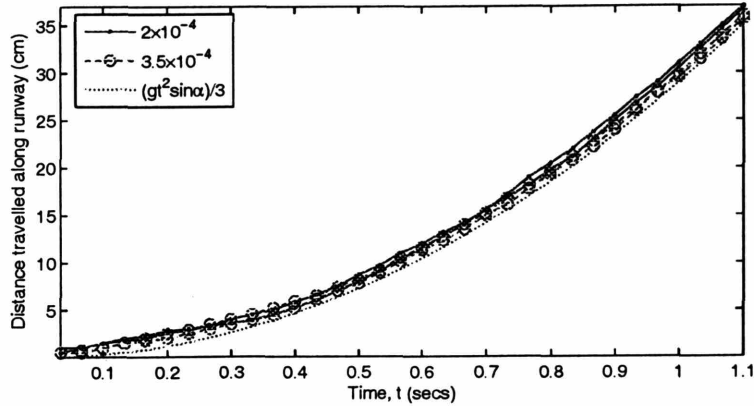


Figure 2-2: Distance traveled along the runway for an aluminum inner cylinder with a slope of 5° . Four experiments are shown: a first pair of repeated runs with $\nu = 2 \times 10^{-4}$ (dots and solid lines), and a second pair with $\nu = 3.5 \times 10^{-4}$ (circles and dashed lines). Also shown is the function, $(gt^2 \sin \alpha)/3$, expected for a solid cylinder (dotted lines).

2.1.2 Observations

Depending on the inclination of the runway, two types of characteristic motion are observed: for high slopes, the cylinder accelerates without bound under gravity. When the slope is not so high, there is no such unabated acceleration, and a slower, rocking and rolling motion ensues. The two characteristic motions are illustrated in figures 2-2 and 2-3, respectively, which show the distance traveled along the runway, X , as a function of time, t . In the first case, the cylinder rolls increasingly quickly down the ramp; the motion is largely independent of the fluid viscosity (experiments with different ν are almost identical) and closely follows the law, $X = \frac{1}{3}gt^2 \sin \alpha$, that is expected for a solid cylinder rolling without sliding. Evidently, the object rolls primarily as a rigid body in this high-slope limit.

While the cylinders do not accelerate indefinitely in the low-slope regime, neither do they move steadily; rather, the cylinders roll erratically down the ramp, rocking back and forth as they progress. On average, however, the speed is roughly steady and well-described by a linear fit over long times. The time series shown in figure 2-3 illustrate this behavior; the inset in the first panel shows a detailed short path, and displays the unsteady, rocking progression of the outer cylinder, while the main

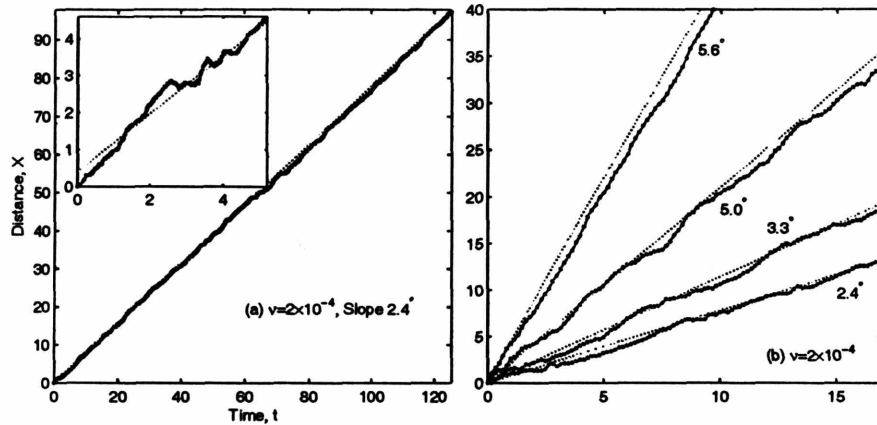


Figure 2-3: Distance traveled along the runway for a steel inner cylinder with various slopes. Panel (a) shows a long run at 2.4°; the inset shows a magnification of the path. Panel (b) shows four different slopes, as marked. The dotted lines show the best-fit linear fits calculated for all the experiments.

picture shows the long-time linear fit.

Observations further show that the rocking corresponds to differential motion between the two cylinders. In particular, throughout the evolution the inner cylinder lies close to its lowest possible point; however, it is dragged up the rear side of the outer cylinder somewhat by the fluid (see figure 2-1); the rocking coincides with irregular sliding of the inner cylinder over the lower surface of the outer one.

2.2 Experiments with the fixed outer cylinder

We next observed a simplified experiment where the rotation rate of the outer cylinder was held constant by a motor to better understand the observed quasi-steady slow rolling motion of the snail cylinders.

2.2.1 Laboratory set-up

An aluminum rod, of length 33.4cm, diameter 2.5cm, and mass 470.2g was placed inside a larger hollow plastic cylinder of length 38.9cm and diameter 10.4cm. (This corresponds to a density of $2.87gcm^{-3}$.) The plastic cylinder was then filled with a

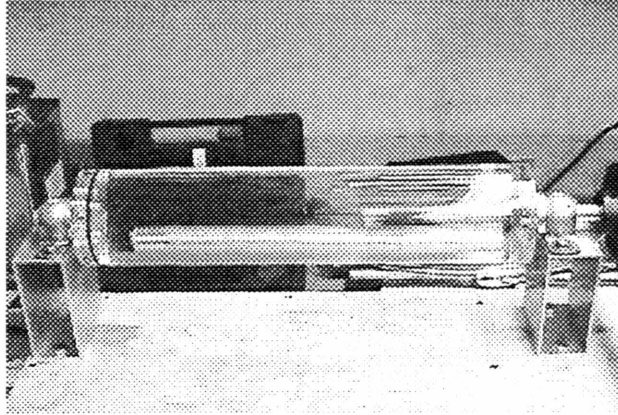


Figure 2-4: The experimental apparatus

viscous fluid and closed. The system was allowed to sit in order to drain off as many of the air bubbles that were trapped in the system as possible. The cylinder was mounted horizontally and attached to a motor, which drove the system by rotating the cylinder along its major axis. Immediately after observing the motion of the inner cylinder, the fluid was collected to record its viscosity and density. The collection was done after the experiment so that we could be reasonably sure of obtaining a homogeneous sample without reintroducing excess air into the container. This process was repeated several times with fluids of different viscosities and densities. The initial experiments were performed with pure Glycerol with viscosity 1186cS and density $1.26gcm^{-3}$. Higher viscosities were achieved with silicon oils by blending 10000cS Dow Corning 200 Fluid with Dow Corning 200 Fluids with viscosities 350cS, 200cS, and 10cS. The observed viscosities ranged between 886cS and 8353cS while the corresponding densities were between $0.953gcm^{-3}$ and $0.969gcm^{-3}$.

2.2.2 Observations

The observed behavior of the inner rod can be divided into five main types as summarized in figure 2-5. These were steady modes, bobbing modes, oscillating modes with changing amplitude, steady oscillating modes, and sticking modes. Generally, these modes occurred in turn as the angular speed increased progressively; however,

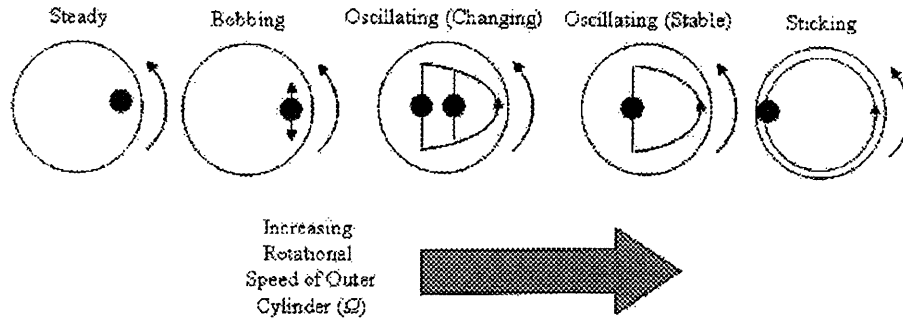


Figure 2-5: The various observed modes. Rotation speed increases from left to right.

all modes were not observed with all fluids. Most notably, for the most viscous fluids, the motor could not be used to generate slow enough speeds to observe more than just the sticking mode; this is most likely due to internal friction within the system.

The steady mode is characterized by the rod remaining stationary at a fixed angular position with respect to the horizontal. The theory of chapter 6 predicts that the center of the rod should lie so that the the line segment between the centers of the cylinders is perpendicular to gravity; however, the rod is observed to lie between 15 and 55 degrees below the horizontal line. The inner rod is not observed to rotate along its own axis of symmetry. When the angular speed of the outer cylinder is increased, the inner cylinder begins to bob. The rod moves principally in the vertical direction, hitting the wall at its highest and lowest points, and also a few *mm* in the horizontal. The range of angles observed at maximum amplitude was 25-45 degrees above the horizontal and 15-40 degrees below. Once again, the rod was not observed to rotate around its axis of symmetry. As the angular speed increases further, the amplitude of the horizontal motion increases; moreover, the motion becomes irregular. This is referred to as the oscillating, changing mode. The rod tends to stick to the outer cylinder, moving with it until it reaches a critical angle above the horizontal. In this mode the critical angle changes between approximately 70 and 110 degrees. Upon reaching its critical angle, the rod's trajectory takes a sharp turn as it falls vertically

towards the bottom of the inner cylinder. When it reaches the bottom this process is repeated. Further increasing the angular speed results in the stable oscillating mode. This mode is similar to the oscillating, changing mode; however, the critical angle above the horizontal, at which the rod falls, remains steady at 110 degrees. In certain experiments, the rod changed directly from the oscillating mode to the sticking mode without an observed stable oscillating mode. Finally, when the angular speed of the outer cylinder exceeds a critical speed, the rod sticks to the wall of the outer cylinder and rotates with it, having been flung out by centripetal forces. We note that in certain experiments, the rod changed directly from the unstable oscillating, changing mode to the sticking mode without an observed stable oscillating mode. Finally, we noticed hysteresis within the system; the transitions between the modes occurred at different spots depending on whether the outer rotation rate was increasing or decreasing.

2.3 Bubbles

It is worth noting that it was very difficult to avoid entraining small air bubbles into the silicon oil when filling both apparatus. We tried to remove as many of these bubbles as possible; however, it was impossible to remove them all because some bubbles remained trapped well away from container openings. In the lower viscosity fluids, the bubbles appeared to collect and merge into one or two bigger bubbles that rose to the top of the fluid and remained there while the cylinders rolled down the runway (as is visible in figure 2-1. In these cases, we did not observe any smaller bubbles collecting in the low pressure regions that occur near the point where the cylinders become closest. However, with the higher viscosity (500 centiStoke) oil, the action of filling and even rapid rolling appeared to create many small bubbles that took several hours to collect together. When the cylinders were rolled down the runway with such “bubbly” oil, we noted a systematic increase of speed of up to 20 percent, especially for higher slopes (see figure 7-4). This is presumably due to reduced dissipation. In these cases, the small bubbles were clearly collecting and in

the narrowest part of the fluid-filled gap, creating a line of cavitation in our system. The total volume of air in the system appears to increase during while the system is in motion. Thus cavitation is clearly dynamically important (though, perhaps, not a dominant effect), as it is in the journal bearing.

Chapter 3

Formulation of the rolling problem

In this chapter, we construct a theoretical model for the snail cylinder's motion. We begin by writing Newton's equations for the force balance on the cylinders. We next change co-ordinates, so that we may simplify the boundary conditions of the fluid dynamics problem that determines the hydrodynamic forces exerted on the cylinders. The lubrication limit is applied to the resulting Navier-Stokes equations allowing us to more readily calculate the viscous force on the cylinders. To close the equations in the model, we consider the total angular momentum in the system. Finally, in section 3.7 we interpret the results of the model in terms of its energetics.

3.1 Geometry

Figure 3-1 illustrates the geometry of interest. A hollow cylinder with center B and radius b contains a smaller solid cylinder with center A and radius a . We use the notation $b = a + \delta$ and assume that $\delta \ll b$. The angular speeds of the inner and outer cylinders are denoted by $\Omega_a(t)$ and $\Omega_b(t)$, respectively. In the narrow gap between the two cylinders there is a viscous fluid with density ρ and kinematic viscosity, ν . The inner and outer cylinders have masses, m_a and m_b , respectively, whereas the fluid has mass $m_f = \pi(b^2 - a^2)L\rho$, with L denoting the axial length of the arrangement. In

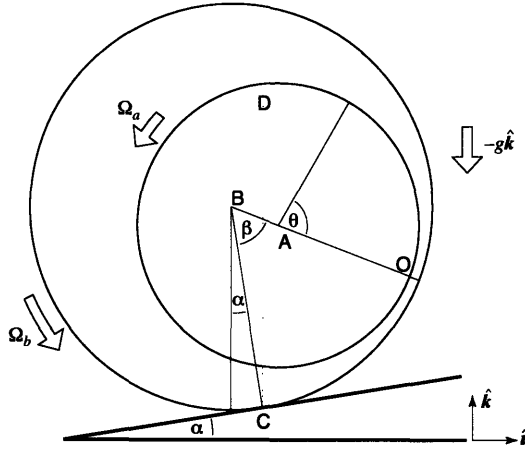


Figure 3-1: The geometry. The point B is the center of the outer, hollow cylinder (radius b) and A is the center of the inner solid cylinder (radius a). The displacement vector from A to B is $\epsilon(t)$. The ‘line of centers’ is BAO . The origin of the gap coordinate system, $(z, \theta) = (0, 0)$ is the point O . If the center of mass of the apparatus lies on vertical line CD then the torque on the right hand side of (3.44) vanishes.

total, the apparatus has mass

$$M \equiv m_a + m_b + m_f . \quad (3.1)$$

The reduced mass of the inner cylinder is $m'_a \equiv m_a - m''_a$, where $m''_a \equiv \pi a^2 L \rho$ is the mass of fluid it displaces.

We use a Cartesian coordinate system attached to a plane inclined at an angle α to the horizontal; the unit vector \hat{s} points up the slope and the unit normal \hat{n} is perpendicular to the plane. The position vector is $\mathbf{X} = X\hat{s} + Z\hat{n}$ and the gravitational acceleration is $-\mathbf{g}$, where

$$\mathbf{g} = g(\sin \alpha \hat{s} + \cos \alpha \hat{n}) . \quad (3.2)$$

In this (X, Z) -coordinate system, the two cylinders have centers at the positions $\mathbf{X}_a = X_a\hat{s} + Z_a\hat{n}$ and $\mathbf{X}_b = X_b\hat{s} + Z_b\hat{n}$, respectively. The requirement that the outer

cylinder rolls without slipping down the plane dictates that

$$\dot{X}_b = -b\Omega_b, \quad Z_b = b. \quad (3.3)$$

Geometry implies that the center of the inner cylinder is given by

$$\mathbf{X}_a = \mathbf{X}_b + \boldsymbol{\epsilon}, \quad \boldsymbol{\epsilon} \equiv \epsilon (\sin \beta \hat{\mathbf{s}} - \cos \beta \hat{\mathbf{n}}). \quad (3.4)$$

Thus the distance between the centers A and B is denoted by $\epsilon(t)$, and $\beta(t)$ is the angle between the line of centers and the perpendicular connecting B to the inclined plane.

Further geometric considerations show that the center of mass of the fluid is at

$$m_f \mathbf{X}_f = m_f \mathbf{X}_b - m_a'' \boldsymbol{\epsilon}. \quad (3.5)$$

Using the relations above, one finds that the center of mass of the whole apparatus, $M \mathbf{X}_c = m_a \mathbf{X}_a + m_b \mathbf{X}_b + m_f \mathbf{X}_f$, is at

$$M \mathbf{X}_c = M \mathbf{X}_b + m_a' \boldsymbol{\epsilon}. \quad (3.6)$$

The relations above express \mathbf{X}_a , \mathbf{X}_f and \mathbf{X}_c in terms of our main independent variables \mathbf{X}_b and $\boldsymbol{\epsilon}$.

3.2 Dynamical equations for the cylinder centers

Considering the motion of the two cylinders we obtain further dynamical relations. In our inertial, (X, Z) -frame, these are

$$m_a \ddot{\mathbf{X}}_a = \mathbf{F}_a - m_a \mathbf{g}, \quad (3.7)$$

and

$$m_b \ddot{\mathbf{X}}_b = \mathbf{F}_b - m_b \mathbf{g} + \mathbf{E}. \quad (3.8)$$

\mathbf{F}_a and \mathbf{F}_b denote the forces that the fluid exerts on the two cylinders. \mathbf{E} is the external force exerted on cylinder B at the point of contact with the plane; this consists of the friction force f_F , acting along the plane, that prevents the outer cylinder from freely sliding downhill, and the normal reaction, f_R , required to hold the cylinder on the plane: $\mathbf{E} = -f_F \hat{s} + f_R \hat{n}$.

The fluid has velocity $\mathbf{U}(X, Z, t)$ and pressure $P(X, Z, t)$, and the Navier-Stokes equation is

$$\rho(\mathbf{U}_t + \mathbf{U} \cdot \nabla \mathbf{U}) = -\nabla P + \rho\nu \nabla^2 \mathbf{U} - \rho\mathbf{g} , \quad (3.9)$$

with $\nabla \equiv (\partial_X, \partial_Z)$. Integration of (3.9) over the gap occupied by the fluid provides a third differential equation for the fluid center of mass, \mathbf{X}_f :

$$m_f \ddot{\mathbf{X}}_f = -\mathbf{F}_a - \mathbf{F}_b - m_f \mathbf{g} . \quad (3.10)$$

Summing (3.7), (3.8) and (3.10) we obtain the total momentum equation of the apparatus

$$M \ddot{\mathbf{X}}_c = \mathbf{E} - M\mathbf{g} . \quad (3.11)$$

The left hand side is the acceleration of the center of mass. The forces on the right of (3.11) include gravity, \mathbf{g} , and the external contact force, \mathbf{E} , introduced above in (3.8).

We now apply the lubrication approximation for the fluid so as to calculate the fluid forces and torques. This approximation is valid provided the gap is thin, and the characteristic Reynolds number ($\text{Re} = b^2 \Omega_b / \nu$) is sufficiently small. Low Reynolds number allows us to neglect fluid accelerations; however, given that the whole apparatus can be in a state of acceleration down the inclined plane, care must be taken in choosing the frame of reference in which to apply the lubrication approximation. The most logical choice is the frame in which the center-of-mass of the fluid remains at rest: in this frame, the average acceleration within the fluid must be zero, so we may expect the local accelerations to be small compared with the pressure and viscous forces per gram throughout the fluid.

Thus we now move to the fluid frame by introducing the transformation

$$\mathbf{x} = \mathbf{X} - \mathbf{X}_f(t), \quad \mathbf{u}(\mathbf{x}, t) = \mathbf{U}(\mathbf{X}, t) - \dot{\mathbf{X}}_f(t), \quad p = P + \rho(\mathbf{g} + \ddot{\mathbf{X}}_f) \cdot \mathbf{x}. \quad (3.12)$$

We recast (3.9) into the form,

$$\rho(\mathbf{u}_t + \mathbf{u} \cdot \nabla \mathbf{u}) = -\nabla p + \rho\nu \nabla^2 \mathbf{u}, \quad (3.13)$$

where now $\nabla \equiv (\partial_x, \partial_z)$. We may now solve the lubrication problem in the gap, as described in section 3.3, and so obtain the fluid force on the cylinders stemming from the viscous flow within the gap. Denoting these viscous forces by \mathbf{f}_a and \mathbf{f}_b , we have $\mathbf{f}_a = -\mathbf{f}_b$, and the total hydrodynamic forces are

$$\mathbf{F}_a = \mathbf{f}_a + m_a''(\mathbf{g} + \ddot{\mathbf{X}}_f) \quad \text{and} \quad \mathbf{F}_b = -\mathbf{f}_a - (m_f + m_a'')(\mathbf{g} + \ddot{\mathbf{X}}_f). \quad (3.14)$$

The terms proportional to $\mathbf{g} + \ddot{\mathbf{X}}_f$ in (3.14) follow from integrating P in (3.12) over the surface of each cylinder. Expressions for the components of \mathbf{f}_a are derived below and presented in (3.38) and (3.39).

3.2.1 Motion of the inner center relative to the outer center: the ϵ equation

Using (3.14) to replace \mathbf{F}_a in (3.7), and (3.4) to eliminate \mathbf{X}_a , gives

$$m_e \ddot{\epsilon} = \mathbf{f}_a - m_a' \mathbf{g} + m_a' b \hat{\Omega}_b \hat{\mathbf{s}}, \quad (3.15)$$

where the effective inertial mass m_e of the inner cylinder is

$$m_e \equiv m_a + \frac{m_a''^2}{m_f}. \quad (3.16)$$

As made more apparent below in section 3.3, in the lubrication problem, the fluid flow in the gap is determined purely by the instantaneous speeds of the cylinders.

Because the natural coordinates that describe the relative motion of the centers of the cylinder are ϵ and β , it is then convenient to represent the hydrodynamic force as

$$\mathbf{f}_a = f_\epsilon \hat{\boldsymbol{\epsilon}} + f_\beta \hat{\boldsymbol{\beta}}. \quad (3.17)$$

f_ϵ and f_β denote the components of the hydrodynamic force on the inner cylinder. The unit vector $\hat{\boldsymbol{\epsilon}} = \boldsymbol{\epsilon}/|\boldsymbol{\epsilon}|$ is directed from B to A (increasing ϵ); $\hat{\boldsymbol{\beta}}$ is perpendicular to $\hat{\boldsymbol{\epsilon}}$ and oriented in the direction of increasing β . Now we resolve the equation of motion of the inner cylinder (3.15) in terms of these polar variables centered on B :

$$m_e(\epsilon\ddot{\beta} + 2\dot{\epsilon}\dot{\beta}) = f_\beta - m'_a g \sin(\alpha + \beta) + m'_a b \dot{\Omega}_b \cos \beta, \quad (3.18)$$

and

$$m_e(\ddot{\epsilon} - \epsilon\dot{\beta}^2) = f_\epsilon + m'_a g \cos(\alpha + \beta) + m'_a b \dot{\Omega}_b \sin \beta. \quad (3.19)$$

3.2.2 Rotational equations of motion

The rotations of the two cylinders satisfy the angular equations of motion,

$$\frac{1}{2}m_a a^2 \dot{\Omega}_a = T_a, \quad (3.20)$$

and

$$m_b b^2 \dot{\Omega}_b = T_b - b f_F. \quad (3.21)$$

Here T_a and T_b denote the fluid torques on the two cylinders. Above we have assumed that the inner cylinder is a uniform solid so that the moment of inertia is $m_a a^2/2$, and that B is a cylindrical shell with moment of inertia $m_b b^2$.

3.3 Hydrodynamic forces and torques

For low Reynolds number flow, the hydrodynamic force in (3.17) may be constructed analytically by solving the bi-harmonic equation in the domain between the two solid

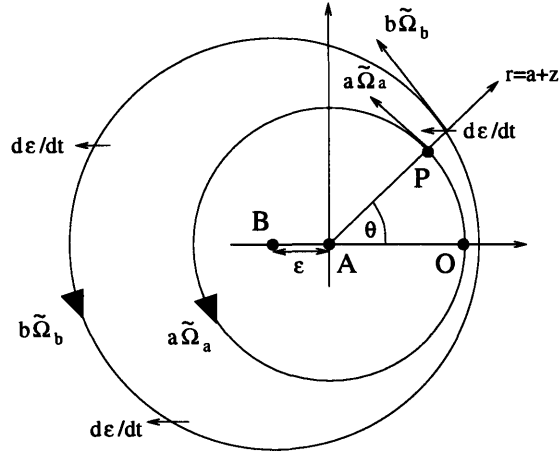


Figure 3-2: The instantaneous speeds associated with points on the surface of the two cylinders.

cylinders[8]. We follow a different route here, however, and make use of the lubrication approximation (that is $\delta \equiv (b - a) \ll a$) to derive a simpler set of relations for the fluid torques and forces.

3.3.1 Lubrication analysis

For lubrication theory, it is convenient to move into a coordinate system in which the centers of the cylinders are not moving and to position a polar coordinate system, (r, θ) , at the inner cylinder (i.e., on point A in figure 3-2). The angle θ is measured positive in the counterclockwise direction with the ray $\theta = 0$ running along the line of centers, BAO , and passing through the narrowest point of the gap. Then the gap width $h(\theta)$ is approximately

$$h(\theta) = \delta - \epsilon \cos \theta, \quad (3.22)$$

where $\delta \equiv b - a \ll a$. We then use a 'gap coordinate', $0 \leq z \leq h(\theta)$, defined by $r \equiv a + z$ so that $(z, \theta) = (0, 0)$ is the point O in Figure 3-1.

To leading order in δ/a , the lubrication equations take the form

$$\rho \nu u_{zz} = a^{-1} p_{\theta}, \quad p_z = 0, \quad \frac{1}{a} u_{\theta} + w_z = 0. \quad (3.23)$$

These must be solved subject to the velocity boundary conditions on the cylinders.

In our new frame of reference, the fluid flow is dictated by the motions of the two cylinders. As shown in figure 3-1, these motions can be divided into the rotations, $\tilde{\Omega}_a = \Omega_a - \dot{\beta}$ and $\tilde{\Omega}_b = \Omega_b - \dot{\beta}$, and a "squeeze flow" in which the outer cylinder moves left with a speed $\dot{\epsilon}$ and compresses the fluid within the narrowest part of the gap. To ease the construction of the fluid forces and torques, we split the lubrication problem into these two parts and construct the full solution via linear superposition. The form of the rotational and squeeze film flows are deduced in sections 3.3.2 and 3.3.3, respectively.

3.3.2 The rotational flow, $u^R(z, \theta)$

To leading order, the boundary conditions are

$$u^R(0, \theta) = a\tilde{\Omega}_a, \quad w^R(0, \theta) = 0, \quad (3.24)$$

and

$$u^R(h, \theta) = a\tilde{\Omega}_b, \quad w^R(h, \theta) = 0. \quad (3.25)$$

The solution is then,

$$u^R(z, \theta) = \left(1 - \frac{z}{h}\right) a\tilde{\Omega}_a + \frac{z}{h} a\tilde{\Omega}_b - \frac{p_\theta^R}{2a\rho\nu} z(h-z). \quad (3.26)$$

An integral of the continuity equation in z then provides the additional condition,

$$\int_0^h u^R(z, \theta) dz = q, \quad (3.27)$$

where q is only a function of time. Introducing $u^R(z, \theta)$ in (3.26) into (3.27) leads to

$$q = \frac{ah}{2} (\tilde{\Omega}_b + \tilde{\Omega}_a) - \frac{h^3 p_\theta^R}{12a\rho\nu}. \quad (3.28)$$

Moreover, since $\oint p_\theta^R d\theta = 0$,

$$q = a\delta(\tilde{\Omega}_b + \tilde{\Omega}_a)\frac{1 - \kappa^2}{2 + \kappa^2}, \quad (3.29)$$

with $\kappa \equiv \epsilon/\delta$. The result (3.29) is obtained using the integrals:

$$\oint \frac{d\theta}{1 - \kappa \cos \theta} = \frac{2\pi}{\sqrt{1 - \kappa^2}}, \quad \oint \frac{d\theta}{(1 - \kappa \cos \theta)^2} = \frac{2\pi}{(1 - \kappa^2)^{3/2}} \quad (3.30)$$

and

$$\oint \frac{d\theta}{(1 - \kappa \cos \theta)^3} = \frac{\pi(2 + \kappa^2)}{(1 - \kappa^2)^{5/2}}. \quad (3.31)$$

Returning to (3.28), and eliminating q with (3.29), we obtain a convenient expression for the dynamic pressure gradient associated with differential rotation in the gap:

$$p_\theta^R(\theta) = \frac{12a^2\rho\nu}{h^3}(\tilde{\Omega}_a + \tilde{\Omega}_b) \left[\frac{h}{2} - \left(\frac{1 - \kappa^2}{2 + \kappa^2} \right) \delta \right]. \quad (3.32)$$

3.3.3 The squeeze flow, $\mathbf{u}^S(z, \theta)$

The boundary conditions are

$$u^S(0, \theta) = w^S(0, \theta) = 0, \quad \text{and} \quad u^S(h, \theta) = \dot{\epsilon} \sin \theta, \quad w^S(h, \theta) = -\dot{\epsilon} \cos \theta, \quad (3.33)$$

from which it follows that

$$u^S(z, \theta) = \frac{z}{h} \dot{\epsilon} \sin \theta - \frac{p_\theta^S}{2a\rho\nu} z(h - z) \quad (3.34)$$

and eventually

$$p^S(\theta) = \frac{6a^2\rho\nu\dot{\epsilon}}{\epsilon h^2}. \quad (3.35)$$

3.3.4 Calculating forces and torques

The viscous force on the inner cylinder is composed of dynamic pressure forces due to the two characteristic fluid motions. In view of our solution obtained in the geometry

of figure 3-1, the dynamic pressure forces are most easily resolved into components acting along and transverse to the line of centers. Recall $\hat{\epsilon}$ denotes the unit vector pointing from B to A , and $\hat{\beta}$ denotes the perpendicular unit vector lying in the direction of increasing β . Then,

$$\mathbf{f}_a = -aL \oint p(\theta)(\hat{\epsilon} \cos \theta + \hat{\beta} \sin \theta) d\theta \equiv f_\epsilon \hat{\epsilon} + f_\beta \hat{\beta}. \quad (3.36)$$

Because of the specific symmetries of the induced pressures, we observe that

$$f_\epsilon = -aL \oint p^S(\theta) \cos \theta d\theta \quad f_\beta = -aL \oint p^R(\theta) \sin \theta d\theta, \quad (3.37)$$

which can be evaluated to yield

$$f_\epsilon = -\frac{12\nu a m_a''}{\delta^2} \frac{\dot{\kappa}}{(1 - \kappa^2)^{3/2}}, \quad (3.38)$$

and

$$f_\beta = \frac{12\nu a m_a''}{\delta^2} \frac{\kappa(\Omega_a + \Omega_b - 2\dot{\beta})}{(2 + \kappa^2)\sqrt{1 - \kappa^2}}, \quad (3.39)$$

where we have defined the non-dimensional distance between the centers by

$$\kappa(t) \equiv \frac{\epsilon(t)}{\delta}. \quad (3.40)$$

Symmetry also demands that the torque on the inner cylinder (about its center) is provided solely by the rotational fluid motion. In particular,

$$T_a \equiv a^2 \rho L \nu \oint u_z^R(0, \theta) d\theta. \quad (3.41)$$

This implies

$$T_a = \frac{12\nu a m_a''}{\delta} \frac{(1 - \kappa^2)(\Omega_b - \dot{\beta}) - (1 + 2\kappa^2)(\Omega_a - \dot{\beta})}{3(2 + \kappa^2)\sqrt{1 - \kappa^2}}. \quad (3.42)$$

In the absence of fluid inertia, the forces on the two cylinders must necessarily

balance. Hence, the hydrodynamic force on the outer cylinder is $\mathbf{f}_b = -\mathbf{f}_a$. Likewise, about any specific fulcrum, the torque on the outer cylinder must be equal and opposite to that on the inner cylinder. Hence, the torque exerted by fluid on the outer cylinder *about its center* (point B) is

$$T_b = -T_a - \epsilon f_\beta. \quad (3.43)$$

(The torque about point B is equivalent to the torque about point A plus the moment of the force about B acting at A .)

3.4 Closing the equations of motion

To obtain a final equation relating the independent variables $[\beta, \epsilon, \Omega_a, \Omega_b]$ we eliminate the friction force f_F between along-plane component of the center of mass momentum equation (3.11) and (3.21). Using (3.6), (3.11),(3.18), (3.20) and (3.43) one can proceed to eliminate all hydrodynamic forces and torques, and so finally obtain an angular momentum equation in terms of $[\beta, \epsilon, \Omega_a, \Omega_b]$:

$$\begin{aligned} \frac{d}{dt} \left[\frac{1}{2} m_a a^2 \Omega_a + (M + m_b) b^2 \Omega_b + m_\epsilon \epsilon^2 \dot{\beta} - m'_a b \frac{d}{dt} (\epsilon \sin \beta) \right] - m'_a b \dot{\Omega}_b \epsilon \cos \beta \\ = M g b \sin \alpha - m'_a g \epsilon \sin(\alpha + \beta). \end{aligned} \quad (3.44)$$

3.4.1 Understanding (3.44) in terms of total angular momentum

The total angular momentum balance about the origin of the (X, Z) -coordinate system boils down to equating the rate of change of total angular momentum to the applied torque. The torque consists of three parts: the moment of the normal reaction at the point of contact, the gravitational torque on the mass $M - m'_a$ centered at B , and the gravitational torque on the mass m'_a centered at A .

At the point of contact between the incline and the outer cylinder, we have

$$X_b f_R \equiv X_b (Mg \cos \alpha + M \ddot{Z}_c). \quad (3.45)$$

Making use of the Z -component of (3.6), i.e.

$$MZ_c \equiv Mb - m'_a \epsilon \cos \beta, \quad (3.46)$$

we have the angular momentum due to the normal reaction:

$$X_b f_R = X_b \left[Mg \cos \alpha - m'_a \frac{d^2}{dt^2} (\epsilon \cos \beta) \right]. \quad (3.47)$$

The gravitational torque on the mass $M - m'_a$ centered at B and on mass m'_a centered at A are

$$Z_b (M - m'_a) g \sin \alpha - X_b (M - m'_a) g \cos \alpha, \quad (3.48)$$

and

$$(b - \epsilon \cos \beta) m'_a g \sin \alpha - X_a m'_a g \cos \alpha, \quad (3.49)$$

respectively. Setting $Z_b = b$ and $Z_a = b - \epsilon \cos \beta$, these torques sum to

$$Mgb \sin \alpha - \epsilon m'_a g \sin(\alpha + \beta) - X_b m'_a \frac{d^2}{dt^2} (\epsilon \cos \beta) \quad (3.50)$$

(taking the anti-clockwise sense as positive).

Similarly, we may account for the angular momentum in the system. It consists of the spin of the two cylinders ($m_a a^2 \Omega_a / 2 + m_b b^2 \Omega_b / 2$), the angular momentum of the shell around B ($m_b b^2 \Omega_b$), the angular momentum of the inner cylinder around A ($m_a [\dot{Z}_a X_a - \dot{X}_a Z_a]$), and the angular momentum of the fluid around X_f ($m_f [\dot{Z}_f X_f - \dot{X}_f Z_f]$).

Totaling up the contributions of the angular moment gives

$$\frac{1}{2} m_a a^2 \Omega_a + (M + m_b) b^2 \Omega_b + \left(m_a + \frac{m_a'^2}{m_f} \right) \epsilon^2 \dot{\beta}$$

$$-m'_a \left[b \frac{d}{dt}(\epsilon \sin \beta) + X_b \frac{d}{dt}(\epsilon \cos \beta) + b \Omega_b \epsilon \cos \beta \right] \quad (3.51)$$

We may now equate the time derivative of (3.51) with (3.50) to arrive at (3.44).

If the apparatus is in a state of uniform rotation then all of the angular accelerations on the left hand side of (3.44) vanish. The remaining terms in (3.44), namely $Mb \sin \alpha = m'_a \epsilon \sin(\alpha + \beta)$, imply that the center of mass \mathbf{X}_c lies on the vertical line CD in Figure 3-1: $(\mathbf{X}_c - X_b \hat{\mathbf{s}}) \times \mathbf{g} = 0$. Thus, consistent with the assumed uniform rotation, the gravitational torque about the point of contact C vanishes. This shows that (3.44) is best interpreted as the angular momentum equation with reference to the contact point C in figure 3-1 as its center of rotation.

To summarize, the motion of the snail cylinder is described by four main independent variables: two angular speeds $\Omega_a(t)$ and $\Omega_b(t)$, and the relative coordinates $\beta(t)$ and $\epsilon(t)$. Lubrication theory in the gap provides expressions for the forces f_κ and f_β in (3.38) and (3.39); the viscous torque on the inner cylinder is T_a in (3.42). Then, (3.18), (3.19), (3.20) and (3.44) is a closed sixth-order system for $[\beta, \epsilon, \Omega_a, \Omega_b]$.

3.5 A steady solution

In chapter 2 we observed that the snail cylinder could hold steady without rolling for inclines of sufficiently low slope. Setting $\Omega_a = \Omega_b = 0$ and taking all time derivatives to be zero, (3.18),(3.19), and (3.44) become

$$f_\beta - m'_a g \sin(\alpha + \beta) = 0, \quad (3.52)$$

$$f_\epsilon + m'_a g \cos(\alpha + \beta) = 0, \quad (3.53)$$

$$Mgb \sin \alpha - m'_a g \epsilon \sin(\alpha + \beta) = 0. \quad (3.54)$$

Since we have taken $\dot{\kappa} = 0$, (3.53) and (3.38) imply that $\epsilon = \delta$ so that we may solve for $\alpha + \beta$ in (3.54) to get

$$\alpha + \beta = \sin^{-1} \left(\frac{b \sin \alpha M}{\delta m'_a} \right). \quad (3.55)$$

We may interpret this steady configuration in terms of a static force balance by observing that f_β and f_ϵ act as static friction forces, opposing motion in the $\hat{\beta}$ and $\hat{\epsilon}$ directions, respectively. This interpretation makes sense since

$$\partial f_\beta / \partial \dot{\beta}, \partial f_\epsilon / \partial \dot{\kappa} < 0. \quad (3.56)$$

Furthermore, since both f_β and f_ϵ are proportional to ν , the fluid viscosity is analogous to a coefficient of static friction. Therefore, we expect that the snail cylinder can hold still at steeper inclines when higher viscosity fluids are used in its construction. The maximum value of α for which the steady configuration can be found at any finite viscosity is determined by (3.55) and is

$$\alpha < \sin^{-1} \left(\frac{m'_a \delta}{M b} \right). \quad (3.57)$$

3.6 A quasi-steady solution

In an “equilibrium solution,” the cylindrical apparatus rolls down the inclined plane at constant speed. That is, all angular accelerations vanish ($\dot{\Omega}_a = \dot{\Omega}_b = \ddot{\beta} = T_a = 0$). The two cylinders maintain constant separation so that $\dot{\kappa} = \dot{\beta} = 0$. With $\dot{\kappa} = 0$ it follows from (3.38) that there is no radial hydrodynamic force: $f_\epsilon = 0$. Then since $\dot{\beta} = 0$ it follows from (3.19), $\alpha + \beta = \pi/2$. In other words, the line of centers is necessarily horizontal. This condition simplifies (3.18) to

$$f_\beta = m'_a g, \quad (3.58)$$

and then (3.44) implies that

$$M b \sin \alpha = m'_a \epsilon = m'_a \delta \kappa. \quad (3.59)$$

An alternative interpretation of this relation is that the total moment must vanish of all forces acting about a fulcrum at the point of contact between the outer cylinder

and inclined plane.

The vanishing of the fluid torque T_a in (3.42) and (3.20) signifies that

$$\Omega_b = \frac{1 + 2\kappa^2}{1 - \kappa^2} \Omega_a. \quad (3.60)$$

The expression for f_ϵ , together with (3.58), now implies the rolling speed,

$$\Omega_b = \frac{m_a g \delta^2}{12\pi\rho\nu L a^3} \frac{(1 + 2\kappa^2)\sqrt{1 - \kappa^2}}{\kappa}, \quad (3.61)$$

which is a monotonically decreasing function of κ over the relevant physical range ($0 \leq \kappa \leq 1$).

The resulting equilibrium, with its curious horizontal line of centers, is equivalent to the classical Sommerfeld solution in the lubrication theory of the journal bearing[13]. A further important feature of this equilibrium is that, according to (3.59), as the slope decreases, so must the separation of the cylinder centers, $\epsilon = \delta\kappa$. Consequently, the rotation rate, Ω_b , *increases* as we reduce the slope. Both of these deductions (horizontal line of centers and increasing rotation with reducing slope) sound unrealistic and are, in fact, at odds with the observations reported in chapter 2. As we indicate later, for physically relevant parameter values, the Sommerfeld equilibrium is not realizable since it is unstable, and different kinds of solutions are observed instead.

3.7 Energetics

An energy equation can be derived from (3.18), (3.19), (3.20) and (3.44):

$$\begin{aligned} \frac{1}{2} \frac{d}{dt} \left\{ m'_a (\dot{X}_a^2 + \dot{Z}_a^2) + I_a \Omega_a^2 + [(M - m'_a)b^2 + I_b] \Omega_b^2 + (m''_a + m_f) \frac{m''_a}{m_f} [(\dot{X}_a - \dot{X}_b)^2 + \dot{Z}_a^2] \right\} \\ = \frac{d}{dt} [m'_a g \epsilon \cos(\alpha + \beta) - Mg X_b \sin \alpha] - \mathcal{D}^S - \mathcal{D}^R. \end{aligned} \quad (3.62)$$

The left-hand side of this relation corresponds to the change in total kinetic energy (with the moments of inertia, I_a and I_b , explicitly written in). The first gravitational

term on the right corresponds to the increase in potential energy as the inner cylinder adjusts its position inside the outer one, whereas the second represents the loss as the whole apparatus moves down the inclined plane. The final combination,

$$\mathcal{D}^S + \mathcal{D}^R \equiv \epsilon(\Omega_b - \dot{\beta})f_\beta + T_a(\Omega_b - \Omega_a) - \dot{\epsilon}f_\epsilon, \quad (3.63)$$

is the energy dissipation rate in the fluid.

We may check (3.63) by returning to the lubrication theory in section 3.3. The mechanical energy dissipation in the gap between the cylinders is given by

$$\mathcal{D} = \rho\nu La \oint \int_0^h u_z^R(z, \theta)^2 dz. \quad (3.64)$$

Due to the angular symmetry we can decompose the dissipation into its rotational and squeeze flow components, $\mathcal{D} = \mathcal{D}^R + \mathcal{D}^S$. Taking the rotational part, we find

$$\rho\nu \oint \int_0^h u_z^R(z, \theta)^2 dz d\theta = \rho\nu a^2 (\tilde{\Omega}_b - \tilde{\Omega}_a)^2 \oint \frac{d\theta}{h} + \frac{1}{2}(\tilde{\Omega}_b + \tilde{\Omega}_a) \oint hp_\theta^R d\theta. \quad (3.65)$$

Evaluating the integrals, one has

$$\mathcal{D}^R = \frac{2\pi\rho\nu La^3}{\delta} \left[\frac{(2 + \kappa^2)(\tilde{\Omega}_b - \tilde{\Omega}_a)^2 + 3\kappa^2(\tilde{\Omega}_b + \tilde{\Omega}_a)^2}{(2 + \kappa^2)\sqrt{1 - \kappa^2}} \right] \quad (3.66)$$

A similar calculation gives

$$\mathcal{D}^S = \frac{12\pi\rho\nu La^3}{\delta} \frac{\dot{\kappa}^2}{(1 - \kappa^2)^{3/2}}, \quad (3.67)$$

for the squeeze flow contribution. Noting (3.38)-(3.42), adding these contributions together verifies (3.63).

We have modeled the snail cylinder with a sixth-order system of differential equations for the free physical variables in the system. This model was then interpreted in terms of its energetics which will be useful in understanding the consequences of the model. In the next chapter, we will non-dimensionalize this system in order to create

a computational model whose predictions can be compared with our observations from chapter 2.

Chapter 4

A reduced lubrication model

In this chapter, we determine non-dimensional quantities that will allow us to model the snail cylinder computationally and describe its dynamics in terms of three non-dimensional quantities. The Sommerfeld equilibrium is discussed and discarded as an explanation for the quasi-steady mode observed in chapter 2. We are able to produce numerical solutions that predict the rocking and the unbounded accelerating modes; however, we find that we must expand the model to encapsulate the quasi-steady rolling.

4.1 Reduction of the dynamics

The equations of motion in (3.18), (3.19), (3.20) and (3.44), and the hydrodynamic quantities defined in (3.38) through (3.42), comprise a sixth-order dynamical system. However, we have already chosen the lubrication limit in which $\delta/a \rightarrow 0$. Moreover, unless the slope is small, the cylinder accelerates downhill without bound. Hence we focus on the distinguished limit in which also $\sin \alpha \sim \delta/a$. In this limit, the sixth-order dynamics is systematically simplified by first non-dimensionalizing using the time scale,

$$\tau_s \equiv 12 \frac{m_a'' \nu a}{m_a' \delta^2 g}. \quad (4.1)$$

The definition of τ_s is motivated by taking the case $\alpha = 0$ and allowing the inner cylinder to settle along the vertical diameter of the outer cylinder; τ_s in (4.1) then corresponds to the settling time.

Using τ_s , we introduce dimensionless variables

$$(\hat{\Omega}_a, \hat{\Omega}_b) \equiv \tau_s(\Omega_a, \Omega_b), \quad (4.2)$$

and a dimensionless time $\hat{t} \equiv t/\tau_s$. It is also convenient to introduce

$$\varphi \equiv \alpha + \beta. \quad (4.3)$$

Then, suppressing the hats, the dimensionless version of (3.20) is

$$\frac{1}{2}\Upsilon\dot{\Omega}_a = \frac{(1 - \kappa^2)(\Omega_b - \dot{\varphi}) - (1 + 2\kappa^2)(\Omega_a - \dot{\varphi})}{3(2 + \kappa^2)\sqrt{1 - \kappa^2}}. \quad (4.4)$$

To leading-order in δ/a , (3.18), (3.19) and (3.44) yield, respectively,

$$\frac{\dot{\kappa}}{(1 - \kappa^2)^{3/2}} = \cos \varphi, \quad (4.5)$$

$$\frac{\kappa(\Omega_a + \Omega_b - 2\dot{\varphi})}{(2 + \kappa^2)(1 - \kappa^2)^{1/2}} = \sin \varphi, \quad (4.6)$$

and

$$\mu\Upsilon\dot{\Omega}_b + \frac{1}{2}\Upsilon\dot{\Omega}_a = s - \kappa \sin \varphi. \quad (4.7)$$

In (4.4), (4.5), (4.6) and (4.7) terms of order δ/a have been neglected, but the dimensionless combinations:

$$\mu \equiv \frac{M + m_b}{m_a}, \quad \Upsilon \equiv \frac{g\delta^3}{144\nu^2} \frac{m_a m'_a}{m_a''^2}, \quad s \equiv \frac{a \sin \alpha}{\delta} \frac{M}{m'_a}, \quad (4.8)$$

are taken to be of $O(1)$. Rough estimates of the size of these combinations based on numbers suitable for the snail ball and cylinders indicates that this choice is reasonable: according to the values listed in Tables 2.1 and 2.2, Υ roughly lies in the range 10^{-2} to 5, whereas s ranges from 0.1 to 1.

4.2 An useful recasting of the reduced system

Here we rewrite the reduced equations in a form that will more easily allow us to look at the linear stability of any of the system's fixed "equilibria." Let us define

$$\Omega_{\pm} = \frac{1}{2}(\Omega_a \pm \Omega_b). \quad (4.9)$$

Some algebraic manipulation allows us to rewrite (4.4) - (4.7) in the following form:

$$\dot{\kappa} = (1 - \kappa^2)^{3/2} \cos \varphi \quad (4.10)$$

$$\dot{\varphi} = \Omega_+ - \frac{1}{2} \frac{(2 + \kappa^2) \sqrt{1 - \kappa^2}}{\kappa} \sin \varphi \quad (4.11)$$

$$\dot{\Omega}_- = -\frac{s}{2\mu\Upsilon} - \frac{1 + 2\mu}{6\mu\Upsilon} \frac{\Omega_-}{(1 - \kappa^2)^{1/2}} + \frac{1 - 2\mu}{4\mu\Upsilon} \kappa \sin \varphi \quad (4.12)$$

$$\dot{\Omega}_+ = \frac{s}{2\mu\Upsilon} + \frac{1 - 2\mu}{6\mu\Upsilon} \frac{\Omega_-}{(1 - \kappa^2)^{1/2}} - \frac{1 + 2\mu}{4\mu\Upsilon} \kappa \sin \varphi. \quad (4.13)$$

In the following discussion, we will find this restatement of the dynamical equations useful when analyzing the system near some special solutions.

4.3 The sedimenting solution with $s = 0$

The reduction in (4.4)-(4.7) was motivated by the "sedimenting solution" that arises when $s = 0$; i.e., the snail ball is on a horizontal plane. If the initial condition is $\Omega_a(0) = \Omega_b(0) = \varphi(0) = 0$ but $\kappa(0) = \kappa_0$ then the reduced model has an analytic solution $\Omega_a(t) = \Omega_b(t) = \varphi(t) = 0$ for all t , and $\kappa(t)$ is obtained from the differential equation

$$\frac{\dot{\kappa}}{(1 - \kappa^2)^{3/2}} = 1, \quad (4.14)$$

with solution,

$$\kappa = \frac{t + \kappa_0 / \sqrt{1 - \kappa_0^2}}{\sqrt{1 + \left(t + \kappa_0 / \sqrt{1 - \kappa_0^2}\right)^2}}. \quad (4.15)$$

In other words, the inner cylinder falls vertically through the center of the outer cylinder and ultimately settles onto the bottom surface. It takes infinite time, however, for contact to occur. This result is equivalent to some well-known lubrication solutions for sedimentation [13].

4.4 Solutions with $s \neq 0$

We proceed by examining the stability of an equilibrium solution that arises on a finite slope, i.e. $s \neq 0$.

4.4.1 The Sommerfeld equilibrium

The Sommerfeld equilibrium in the reduced model takes the simple form,

$$\kappa = s, \quad \varphi = \frac{\pi}{2}, \quad \Omega_a = \frac{1-s^2}{1+2s^2}\Omega_b, \quad \Omega_b = s^{-1}\sqrt{1-s^2}(1+2s^2). \quad (4.16)$$

Note that $\varphi = \pi/2$ indicates that the center axes of symmetry of the inner and outer cylinders lie in the same horizontal plane. In terms of our symmetric angular velocity variables in (4.10) - (4.13), we have

$$\Omega_- = -\frac{3}{2}s\sqrt{1-s^2}, \quad \Omega_+ = \frac{(1+2s^2)\sqrt{1-s^2}}{2s}. \quad (4.17)$$

To study the behavior near the Sommerfeld equilibrium we define

$$\eta \equiv \kappa - s, \quad \zeta \equiv \varphi - \frac{\pi}{2}, \quad \omega_- \equiv \Omega_- + \frac{3s\sqrt{1-s^2}}{2}, \quad \omega_+ \equiv \Omega_+ - \frac{(2+s^2)\sqrt{1-s^2}}{2}, \quad (4.18)$$

so that when we linearize (4.10)-(4.11)

$$\begin{pmatrix} \dot{\eta} \\ \dot{\zeta} \\ \dot{\omega}_- \\ \dot{\omega}_+ \end{pmatrix} = \begin{pmatrix} 0 & -(1-s^2)^{3/2} & 0 & 0 \\ \frac{2s^4-s^2+2}{2s^2\sqrt{1-s^2}} & 0 & 0 & 1 \\ \frac{1-2\mu+4\mu s^2}{4\mu\Upsilon(1-s^2)} & 0 & -\frac{1+2\mu}{6\mu\Upsilon\sqrt{1-s^2}} & 0 \\ -\frac{1+2\mu-8\mu s^2}{4\mu\Upsilon(1-s^2)} & 0 & \frac{1-2\mu}{6\mu\Upsilon\sqrt{1-s^2}} & 0 \end{pmatrix} \begin{pmatrix} \eta \\ \zeta \\ \omega_- \\ \omega_+ \end{pmatrix}. \quad (4.19)$$

Therefore, we have reduced the question of the stability of the system around the Sommerfeld equilibrium to calculating the eigenvalues of a 4 by 4 matrix. That is, we must ask whether or not the matrix in (4.19) has an eigenvalue which has a positive real part. Recall that the eigenvalues of a matrix A satisfy the equation $\det(A - \lambda I) = 0$, so that we must determine the roots of the following:

$$\lambda^4 + \frac{1 + 2\mu}{6\mu\Upsilon\sqrt{1-s^2}}\lambda^3 + \frac{2 - 3s^2 + 3s^4 - 2s^6}{2s^2}\lambda^2 + \frac{\sqrt{1-s^2}((1-s^2)^2 + \mu(2-4s^2+8s^4))}{6\mu\Upsilon s^2}\lambda - \frac{1-s^2}{3\mu\Upsilon^2} = 0. \quad (4.20)$$

We can easily verify that, for all $0 \leq s < 1$,

$$\frac{1 + 2\mu}{6\mu\Upsilon\sqrt{1-s^2}}, \frac{2 - 3s^2 + 3s^4 - 2s^6}{2s^2}, \frac{\sqrt{1-s^2}((1-s^2)^2 + \mu(2-4s^2+8s^4))}{6\mu\Upsilon s^2}, \frac{1-s^2}{3\mu\Upsilon^2} \geq 0. \quad (4.21)$$

Therefore, by Descartes's Rule of Signs, (4.20) must have exactly one positive real root, and the equilibrium is unstable.

4.4.2 Other solutions

There is another special solution of (4.4)-(4.7), namely the “pushed pendulum motion”, which is characterized by

$$\kappa = 1, \quad \Omega_{\mathbf{a}} = \Omega_{\mathbf{b}} = -\dot{\varphi}. \quad (4.22)$$

$\varphi(t)$ is then obtained from

$$\Upsilon(\mu + \frac{1}{2})\ddot{\varphi} + s + \sin \varphi = 0. \quad (4.23)$$

This system is conservative because the gap is closed when $\kappa = 1$, and the fluid and cylinders behave like a solid body. That is, there is no relative motion between the fluid and the cylinders and the apparatus is effectively an eccentrically weighted solid cylinder on an inclined plane. Thus, there is either acceleration down (if $s > 1$), or if s is small the apparatus can sit stably at the bottom of a stable energy well.

The stability of the solid-body solutions can be determined as follows: First we

set $\zeta = \sqrt{1 - \kappa^2} \ll 1$. Then, it follows from model equations that

$$\dot{\zeta} = -\zeta^2 \cos \varphi + O(\zeta^3) \quad (4.24)$$

and

$$\Upsilon(\mu + \frac{1}{2})\ddot{\varphi} + s + \sin \varphi = 3\Upsilon^2(\mu^2 + \frac{1}{4})\zeta \frac{d^3\varphi}{dt^3} + O(\zeta^2). \quad (4.25)$$

These equations can be solved by the method of multiple scales. Of special interest is the fixed point, $\sin \varphi = -s$ and $\Omega_a = \Omega_b = 0$, whose stability can be determined by linearization in (4.24) and (4.25):

$$\dot{\zeta} \approx -\zeta^2 \sqrt{1 - s^2}, \quad \Upsilon(\mu + \frac{1}{2}) \frac{d^2\check{\varphi}}{dt^2} + \sqrt{1 - s^2}\check{\varphi} \approx 3\Upsilon^2(\mu^2 + \frac{1}{4})\zeta \frac{d^3\check{\varphi}}{dt^3}, \quad (4.26)$$

where $\check{\varphi} = \varphi - \sin^{-1} s$. The multiple-scale solution is

$$\zeta = \frac{\zeta(0)}{1 + t\zeta(0)\sqrt{1 - s^2}}, \quad \check{\varphi} = \left[1 + t\zeta(0)\sqrt{1 - s^2}\right]^{-q} e^{i\omega t} + c.c., \quad (4.27)$$

with

$$\omega^2 = \frac{\sqrt{1 - s^2}}{\Upsilon(\mu + \frac{1}{2})}, \quad q = \frac{3(1 + 4\mu^2)}{2(1 + 2\mu)^2},$$

indicating that this special point is always stable. However, being stationary, this special solution cannot explain a slow migration down the plane with constant speed.

4.4.3 Numerical solutions

To progress further, we solve the reduced model numerically by integrating the equations with a varying time-step Runge-Kutta method. Two characteristic types of solutions are obtained: First, when s is not too large, solutions settle vertically through the fluid, rocking back and forth, and rolling somewhat downhill; see figure 4-1. Ultimately the inner cylinder sediments onto the outer one, with a limiting solution, $\kappa \rightarrow 1$, $(\Omega_a, \Omega_b) \rightarrow 0$ and $\sin \varphi \rightarrow s$.

Second, when s is too large (exceeding a value just below unity, and depending on the initial condition), the solution locks into a runaway rolling solution as illustrated

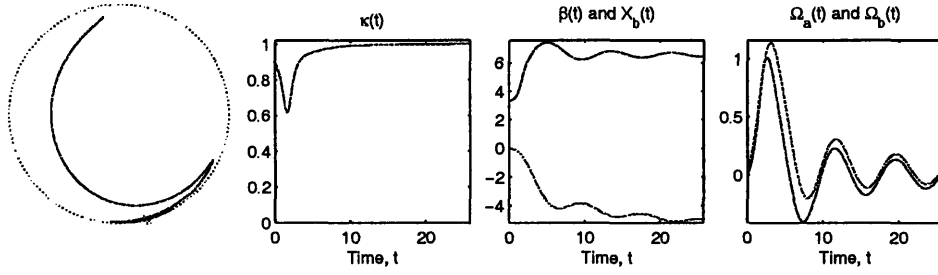


Figure 4-1: Sample rocking solution with $\Upsilon = 1$, $m_b = 0$ ($M = m_a$) and $s = 1/4$. The panels show (a) the locus of the center of the inner cylinder on the polar (κ, β) plane (with $\beta = 0$ pointing vertically downwards), (b) $\kappa(t)$, (c) $\beta(t)$ and $X_b(t)$ (blue and red, respectively), and (d) $\Omega_a(t)$ and $\Omega_b(t)$ (blue and red, respectively). The initial position of the inner cylinder is shown, and $\Omega_a(0) = \Omega_b(0) = 0$. The star in the polar plot marks the limiting sedimentation solution.

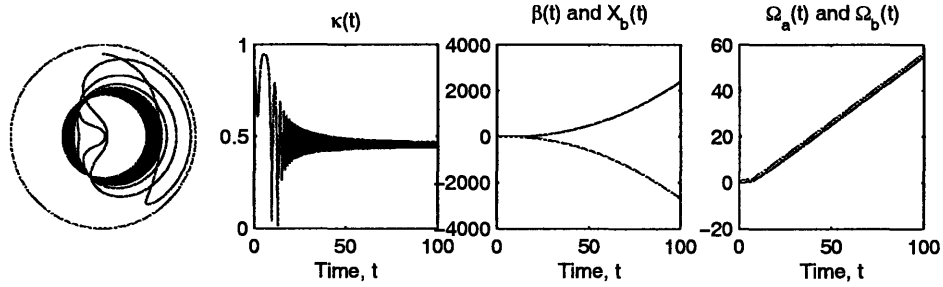


Figure 4-2: Sample runaway solution with $\Upsilon = 1$, $m_b = 0$ ($M = m_a$) and $s = .9$. The layout of the figure is largely as in figure 4-1. The cylinders are initially at rest.

in figure 4-2. The runaway solution has the limiting form, $\Omega_a \sim \Omega_b \sim \dot{\varphi} \sim t$ and κ approaches a constant determined by the initial conditions; aside from some rapidly oscillating factors,

$$\Omega_b \sim \frac{2m_a s t}{M + m_b + 2m_a}. \quad (4.28)$$

Over a range of s , both rocking and rolling solutions are possible; which one emerges is selected by the initial condition. The sedimenting, rocking solution disappears for $s \geq 1$ (since then $\sin \varphi < s$), and only runaway solutions are possible beyond that critical slope. The unbounded accelerating solution, on the other hand, appears to persist at relatively small values of s , although the initial conditions that generate the runaway solution become rather extreme.

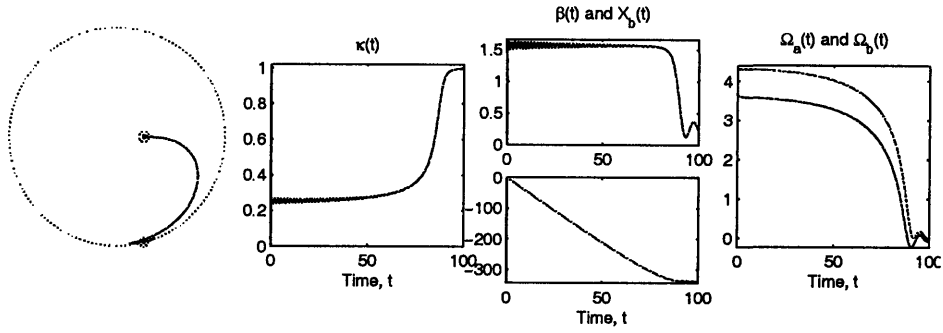


Figure 4-3: Instability of the Sommerfeld solution for $\Upsilon = 1$, $m_b = 0$ and $s = 1/4$. The layout of the figure is largely as in figure 4-1. Initial conditions are chosen very close to the Sommerfeld fixed point (indicated by the circle).

Finally, we expose the fate of a solution starting near the Sommerfeld solution. Figure 4-3 shows an initial-value problem in which the solution is kicked off near the fixed point. Although the system remains near the fixed point for several full rotations of the outer cylinder, ultimately it diverges from that equilibrium, revealing it to be an unstable solution; hence, it cannot provide a means by which to rationalize the observed quasi-steady mode. Since the Sommerfeld solution is not stable, it is not physically realizable despite its apparent similarity with our observations. However, the Sommerfeld equilibrium predicts steady acceleration and an exact balance between the reduced gravity and viscous forces yielding $\varphi = \pi/2$; neither of these are characteristic of the quasi-steady rolling.

4.5 Shortcomings of the model

The rocking and runaway rolling solutions we have generated with the model explain only some of the snail cylinder's observed behavior. Furthermore, since the Sommerfeld solution is unstable, we cannot use it to rationalize the quasi-static slow rolling which accounted for our initial interest in the problem. Nevertheless, these issues reveal a significant flaw in the theory: in the rocking solutions, the inner cylinder continually sediments and the rocking slows down as the gap between the cylinders thins. In contrast, the observed quasi-steady rolling motion becomes roughly steady.

Hence there must be additional physical effects that halt sedimentation and allow roughly steady rolling.

In chapters 5 and 6, we consider a similar physical system with one less degree of freedom; namely, we force Ω_b to be a constant. This will lead us to consider two possible explanations for the quasi-steady rolling in chapter 8: a rough contact between the surface that limits the thinness of the gap, and cavitation near the point of contact.

Chapter 5

Theoretical formulation of the stationary mixer problem

In this chapter, we develop a theoretical model for the simplified experiments discussed in chapter 2, in which the outer cylinder's rotation rate was held constant. We develop a fifth-order system of differential equations to describe the motion of the inner cylinder in this system. We apply the results of Finn and Cox [8] in order to avoid relying on the lubrication limit assumed for the snail cylinders in chapters 3 and 4.

5.1 Geometry

We now consider a fixed hollow cylinder, with center B and radius b , containing a smaller solid cylinder with center A , radius a , and mass m_a , as shown in figure 5-1. This system is analogous to the geometry of figure 3-1 with $\alpha = 0$ and $m_b = 0$. Unless noted otherwise, all variables in this chapter are defined in chapter 3. In particular,

$$M \equiv m_a + m_f = m'_a + m''_a + m_f = m'_a + \pi b^2 L \rho \quad (5.1)$$

where $m''_a \equiv \pi a^2 L \rho$ is the mass of fluid displaced by the inner cylinder and $m'_a = m_a - m''_a$ is its reduced mass.

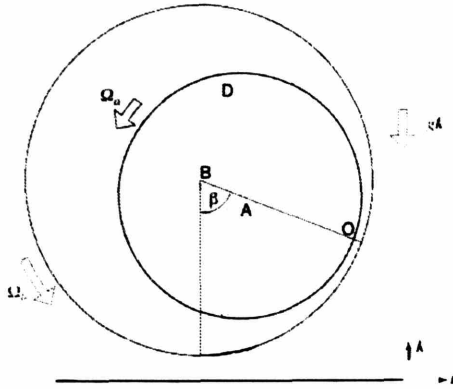


Figure 5-1: The geometry. The point B is the center of the outer, hollow cylinder (radius b) and A is the center of the inner solid cylinder (radius a). The ‘line of centers’ is BAO .

We use a stationary Cartesian coordinate system centered at B , the center of the outer cylinder. \hat{n} and \hat{s} are now unit vectors in the vertical and horizontal directions, respectively. In this frame, the position vector is $\mathbf{X} = X\hat{s} + Z\hat{n}$ and the gravitational acceleration is purely in the vertical direction.

In this (X, Z) -coordinate system, the center of the inner cylinder at time t is taken to be $\mathbf{X}_a(t) = X_a\hat{s} + Z_a\hat{n}$. We define ϵ and β as the distance the center of the inner cylinder is from the center of outer cylinder and the angle that line between those centers makes with $-\hat{n}$, respectively. That is

$$\epsilon \equiv \|\mathbf{X}_a\|, \quad \beta = \arctan\left(-\frac{X_a}{Z_a}\right). \quad (5.2)$$

As previously, we also define unit normal vectors $\hat{e} = \mathbf{X}_a/\epsilon$ and $\hat{\beta}$ so that \hat{e} points in the direction from B to A , and $\hat{\beta}$ is perpendicular to \hat{e} and points in the direction of increasing β . Finally, we remark that the geometry determines the fluid’s center of mass,

$$\mathbf{X}_f = -\frac{m_a''}{m_f}\mathbf{X}_a, \quad (5.3)$$

since B denotes the center of the fluid filled cylinder.

5.2 Dynamic equations for the inner cylinder center

In the inertial, (X, Z) , frame the force balance on the center of the inner cylinder is given by

$$m_a \ddot{\mathbf{X}}_a = \mathbf{F}_a - m_a g \hat{\mathbf{n}}, \quad (5.4)$$

where \mathbf{F}_a denotes the force exerted on the inner cylinder by the fluid. In this inertial frame we can apply the Navier-Stokes momentum equation to the fluid velocity $\mathbf{U}(X, Z, t)$ and its pressure $P(X, Z, t)$. That is,

$$\rho(\mathbf{U}_t + \mathbf{U} \cdot \nabla \mathbf{U}) = -\nabla P + \rho \nu \nabla^2 \mathbf{U} - \rho g \hat{\mathbf{n}}, \quad (5.5)$$

where $\nabla \equiv \partial_X \hat{\mathbf{s}} + \partial_Z \hat{\mathbf{n}}$

Now we intend to calculate the hydrodynamic forces within the system by solving the Stokes flow equations within the fluid. For this approximation of the full Navier-Stokes equations to be valid, the flow must be characterized by low Reynolds number. Therefore, we reformulate the Navier-Stokes equations in the non-inertial reference frame centered at the fluid's center of mass, as we did in chapter 3. In this frame all fluid accelerations must sum to zero.

Thus we transform coordinates so that

$$\mathbf{x} = \mathbf{X} - \mathbf{X}_f(t), \quad \mathbf{u}(\mathbf{x}, t) = \mathbf{U}(\mathbf{X}, t) - \dot{\mathbf{X}}_f(t), \quad p = P + \rho(g \hat{\mathbf{n}} + \ddot{\mathbf{X}}_f) \cdot \mathbf{x}. \quad (5.6)$$

In this reference frame (5.5) is simplified into

$$\rho(\mathbf{u}_t + \mathbf{u} \cdot \nabla \mathbf{u}) = -\nabla p + \rho \nu \nabla^2 \mathbf{u}, \quad (5.7)$$

where now $\nabla = \partial_x \hat{\mathbf{s}} + \partial_z \hat{\mathbf{n}}$. We may now use the solution[8] of this system to determine the viscous pressure forces, due to dynamic p , on the inner cylinder. Let us denote this force by \mathbf{f}_a the components of which are given below in (5.11). By

integrating the total pressure, P , in (5.6) around the surface of the inner cylinder we may summarize our calculation of \mathbf{F}_a as

$$\mathbf{F}_a = \mathbf{f}_a + m_a''(g\hat{\mathbf{n}} + \ddot{\mathbf{X}}_f). \quad (5.8)$$

Plugging (5.8) and (5.3) into (5.4), we now find

$$\left(m_a + \frac{m_a''^2}{m_f}\right) \ddot{\mathbf{X}}_a = \mathbf{f}_a - m_a'g\hat{\mathbf{n}}. \quad (5.9)$$

In light of (5.9), we may define $m_e = m_a + m_a''^2/m_f$ to be the effective mass of the inner cylinder taking into account the added mass of fluid which must be displaced by its motion.

To calculate \mathbf{f}_a , we exploit the summary provided by Finn and Cox [8]. (See Appendix B for a brief synopsis of their methods.) We first define $\kappa = \epsilon/\delta$; in terms of our variables, they find

$$\mathbf{f}_a = f_\epsilon \hat{\boldsymbol{\epsilon}} + f_\beta \hat{\boldsymbol{\beta}} \quad (5.10)$$

$$= \frac{8m_a''\nu\delta}{a^2} \left\{ \frac{(a^2 + b^2 - \epsilon^2)\dot{\kappa}}{2\Delta[1 + (b^2 + a^2 - \epsilon^2)\mathcal{J}]} \hat{\boldsymbol{\epsilon}} - \frac{\kappa[a^2(\Omega_a - \dot{\beta}) + b^2(\Omega_b - \dot{\beta})]}{2\Delta[1 + (b^2 + a^2)\mathcal{J}]} \hat{\boldsymbol{\beta}} \right\} \quad (5.11)$$

where

$$\Delta^2 = (b + a + \epsilon)(b + a - \epsilon)(b - a + \epsilon)(b - a - \epsilon) \quad (5.12)$$

and

$$\mathcal{J} = \frac{1}{2\Delta} \log \left[\frac{(b^2 - a^2 - \epsilon^2 - \Delta)(b^2 - a^2 + \epsilon^2 + \Delta)}{(b^2 - a^2 - \epsilon^2 + \Delta)(b^2 - a^2 + \epsilon^2 - \Delta)} \right]. \quad (5.13)$$

The fluid also exerts a torque on the inner cylinder, due to rotational fluid motion, about its center (point A):

$$T_a = 8m_a''\nu \frac{\epsilon^2(\Omega_a - \dot{\beta}) - b^2[1 + (b^2 + a^2 - \epsilon^2)\mathcal{J}](\Omega_a - \Omega_b)}{2\Delta[1 + (b^2 + a^2)\mathcal{J}]} \quad (5.14)$$

We are now in a position to write a closed system of equations for the motion of the inner cylinder in terms of ϵ , β , and Ω_a . Writing (5.9) in terms of its $\hat{\boldsymbol{\epsilon}}$ and $\hat{\boldsymbol{\beta}}$

components, we have

$$m_e \left(\epsilon \ddot{\beta} + 2\dot{\epsilon} \dot{\beta} \right) = -\frac{8m_a'' \nu \delta}{a^2} \left[\frac{\kappa [a^2(\Omega_a - \dot{\beta}) + b^2(\Omega_b - \dot{\beta})]}{2\Delta[1 + (b^2 + a^2)\mathcal{J}]} \right] - m_a' g \sin \beta \quad (5.15)$$

$$m_e \left(\ddot{\epsilon} - \epsilon \dot{\beta} \right) = \frac{8m_a'' \nu \delta}{a^2} \left[\frac{(a^2 + b^2 - \epsilon^2)\dot{\kappa}}{2\Delta[1 + (b^2 + a^2 - \epsilon^2)\mathcal{J}]} \right] + m_a' g \cos \beta. \quad (5.16)$$

To close the system we write the torque balance on the inner cylinder using (5.14).

That is

$$\frac{1}{2} m_a a^2 \dot{\Omega}_a = 8m_a'' \nu \frac{\epsilon^2(\Omega_a - \dot{\beta}) - b^2[1 + (b^2 + a^2 - \epsilon^2)\mathcal{J}](\Omega_a - \Omega_b)}{2\Delta[1 + (b^2 + a^2)\mathcal{J}]} \quad (5.17)$$

In the following chapter, we non-dimensionalize our model and computationally predict solutions. Comparison with observations reported in chapter 2 will lead us to consider the effects of surface roughness which will be the key to understanding the snail cylinder.

Chapter 6

Dimensionless formulation of the fixed outer cylinder system

Here we shall find the dimensionless parameters that allow us to model our system numerically. We find that the motion can be characterized by only two numerical parameters. The resulting model is then compared with the snail cylinder model of chapter 3. We then proceed by analyzing the consequences of our model for the classical journal bearing problem, in which both Ω_a and Ω_b are held constant. After verifying the predicted results, we produce time series to examine the case where we allow the inner cylinder to rotate freely. Since these predictions do not encapsulate the most interesting aspect of the experiment, namely the fact that the inner cylinder fall onto the outer cylinder wall, we add a sliding contact term that enables the model to better rationalize the observations.

6.1 Determining the dimensionless system

We define a sedimentation time, τ_m , which corresponds to the amount of time needed for the inner cylinder to fall a distance δ ,

$$\tau_m = \frac{8m_a''\nu\delta}{m_a'ga^2}, \quad (6.1)$$

and introduce the dimensionless variables, $\hat{\Omega}_a = \Omega_a \tau$, $\hat{\Omega}_b = \Omega_b \tau$, $t = \tau \hat{t}$, $\hat{\delta} = \delta/a$, $\kappa = \epsilon/\delta$, $\hat{\Delta} = \Delta/a^2$ and $\mathcal{J} = \hat{\mathcal{J}}/a^2$. Then, keeping the hat notation (to reduce confusion when comparing the numerical results to the experiments in chapter 7) while defining $\dot{X} = dX/d\hat{t}$, (5.15)-(5.17) become, respectively

$$\kappa \ddot{\beta} + 2\dot{\kappa}\dot{\beta} = -\gamma \kappa \mathcal{J}_1[\hat{\Omega}_a - \dot{\beta} + (1 + \hat{\delta})^2(\hat{\Omega}_b - \dot{\beta})] - \gamma \sin \beta, \quad (6.2)$$

$$\ddot{\kappa} - \kappa \dot{\beta}^2 = \gamma \mathcal{J}_2(2 + 2\hat{\delta} + \hat{\delta}^2 - \hat{\delta}^2 \kappa^2)\dot{\kappa} + \gamma \cos \beta, \quad (6.3)$$

and

$$\frac{1}{2} \frac{d}{d\hat{t}} \hat{\Omega}_a = \gamma \frac{m_e}{m_a} \hat{\delta}^2 \kappa^2 \mathcal{J}_1(\hat{\Omega}_a - \dot{\beta}) - \gamma \frac{m_e}{m_a} \frac{(1 + \hat{\delta})^2 \mathcal{J}_1}{2\hat{\Delta} \mathcal{J}_2} (\hat{\Omega}_a - \hat{\Omega}_b), \quad (6.4)$$

where

$$\gamma \equiv 64 \frac{m_a''^2 \nu^2 \delta}{m_e m_a' g a^4} = \frac{8m_a'' \nu \tau}{m_e a^2} = \frac{m_a' g \tau^2}{m_e \delta}, \quad (6.5)$$

$$\mathcal{J}_1(\kappa) = \frac{1}{2\hat{\Delta}(\kappa) \left(1 + (2 + 2\hat{\delta} + \hat{\delta}^2)\hat{\mathcal{J}}(\kappa)\right)}, \quad \mathcal{J}_2(\kappa) = \frac{1}{2\hat{\Delta}(\kappa) \left(1 + (2 + 2\hat{\delta} + \hat{\delta}^2 - \hat{\delta}^2 \kappa^2)\hat{\mathcal{J}}(\kappa)\right)}. \quad (6.6)$$

In chapter 3, we derived the following equations describing the motion of a rolling journal bearing, described in figure 3-1.

$$m_e(\epsilon \ddot{\beta} + 2\dot{\epsilon}\dot{\beta}) = f_\beta - m_a' g \sin(\alpha + \beta) + m_a' b \dot{\Omega}_b \cos \beta. \quad (6.7)$$

$$m_e(\ddot{\epsilon} - \epsilon \dot{\beta}^2) = f_\epsilon + m_a' g \cos(\alpha + \beta) + m_a' b \dot{\Omega}_b \sin \beta. \quad (6.8)$$

$$\frac{1}{2} m_a a^2 \dot{\Omega}_a = T_a. \quad (6.9)$$

$$\begin{aligned} \frac{d}{dt} \left[\frac{1}{2} m_a a^2 \Omega_a + (M + m_b) b^2 \Omega_b + m_e \epsilon^2 \dot{\beta} - m_a' b \frac{d}{dt} (\epsilon \sin \beta) \right] - m_a' b \dot{\Omega}_b \epsilon \cos \beta \\ = M g b \sin \alpha - m_a' g \epsilon \sin(\alpha + \beta). \end{aligned} \quad (6.10)$$

In these equations, α is the angle of inclination and m_b is the mass of the outer cylinder. The hydrodynamic forces and torques, f_β , f_ϵ , and T_a were then calculated in the small gap limit.

We may also derive (5.15)-(5.17) from (3.18)-(3.44), by taking $d\Omega_b/dt = 0$, $m_b = 0$, and $\alpha = 0$. The additional external force and torque which must be applied to the outer cylinder in order to keep its rotational speed constant makes (6.10) superfluous. The remaining equations, (6.7)-(6.9), correspond to (5.15)-(5.17). Furthermore, by considering the limit $\delta \rightarrow 0$, in (5.11) and (5.14), we find

$$\Delta \rightarrow 2a\delta\sqrt{1-\kappa^2}, \quad \mathcal{J} \rightarrow -\frac{1}{2a^2}, \quad (6.11)$$

$$f_\kappa \rightarrow -12\pi\rho\nu L \frac{a^3}{\delta^2} \frac{\dot{\kappa}}{(1-\kappa^2)^{3/2}}, \quad f_\beta \rightarrow 12\pi\rho\nu L \frac{a^3}{\delta^2} \frac{\Omega_a + \Omega_b - 2\dot{\beta}}{(2+\kappa^2)\sqrt{1-\kappa^2}} \quad (6.12)$$

and

$$T_i \rightarrow 4\pi\rho\nu L a^3 \frac{(\Omega_b - \dot{\beta})(1-\kappa^2) - (1+2\kappa^2)(\Omega_a - \dot{\beta})}{\delta(2+\kappa^2)\sqrt{1-\kappa^2}}, \quad (6.13)$$

which are in agreement with the lubrication forces calculated to derive (6.7)-(6.10).

6.2 The journal bearing

For this problem, one prescribes the (steady) rotation of the two cylinders, and explores the motion of the inner cylinder under an applied load. With $\hat{\Omega}_a$ and $\hat{\Omega}_b$ prescribed, the equations of motion (6.2)-(6.4) reduce to

$$\kappa\ddot{\beta} + 2\dot{\kappa}\dot{\beta} = -\gamma\kappa\mathcal{J}_1[\hat{\Omega}_a - \dot{\beta} + (1+\hat{\delta})^2(\hat{\Omega}_b - \dot{\beta})] - \gamma\sin\beta \quad (6.14)$$

and

$$\ddot{\kappa} - \kappa\dot{\beta}^2 = \gamma\mathcal{J}_2(2+2\hat{\delta}+\hat{\delta}^2-\hat{\delta}^2\kappa^2)\dot{\kappa} + \gamma\cos\beta, \quad (6.15)$$

since (6.4) is now superfluous. The only fixed point is that with $\beta = \pi/2$ and $\kappa = \kappa_*$ such that

$$\kappa_*\mathcal{J}_1(\kappa_*)[\hat{\Omega}_a + (1+\hat{\delta})^2\hat{\Omega}_b] = -1. \quad (6.16)$$

To check the validity of our model, we shall verify that this fixed point is unstable for any choice of $\hat{\Omega}_a$, $\hat{\Omega}_b$ and $\hat{\delta}$.

We may linearize (6.14) and (6.15) in $\kappa, \beta, \dot{\kappa}$, and $\dot{\beta}$ near this equilibrium to find

$$\ddot{\beta} \approx \gamma \left[\frac{\mathcal{J}'_1(\kappa_*)}{\kappa_* \mathcal{J}_1(\kappa_*)} + \frac{1}{\kappa_*^2} \right] (\kappa - \kappa_*) + \gamma (2 + 2\hat{\delta} + \hat{\delta}^2) \mathcal{J}_1(\kappa_*) \dot{\beta}, \quad (6.17)$$

and

$$\ddot{\kappa} \approx -\gamma \left(\beta - \frac{\pi}{2} \right) + \gamma (2 + 2\hat{\delta} + \hat{\delta}^2 - \delta^2 \kappa_*^2) \mathcal{J}_2(\kappa_*) \dot{\kappa}. \quad (6.18)$$

In matrix form, these correspond to

$$\frac{d}{dt} \begin{pmatrix} \beta \\ \kappa \\ \dot{\beta} \\ \dot{\kappa} \end{pmatrix} = \begin{pmatrix} 0 & 0 & 1 & 0 \\ 0 & 0 & 0 & 1 \\ 0 & \gamma c_{32}(\kappa_*) & -\gamma c_{33}(\kappa_*) & 0 \\ -\gamma & 0 & 0 & -\gamma c_{44}(\kappa_*) \end{pmatrix} \begin{pmatrix} \beta - \pi/2 \\ \kappa - \kappa_* \\ \dot{\beta} \\ \dot{\kappa} \end{pmatrix}, \quad (6.19)$$

where

$$c_{32}(\kappa_*) = \frac{\mathcal{J}'_1(\kappa_*)}{\kappa_* \mathcal{J}_1(\kappa_*)} + \frac{1}{\kappa_*^2} \quad (6.20)$$

$$c_{33}(\kappa_*) = - (2 + 2\hat{\delta} + \hat{\delta}^2) \mathcal{J}_1(\kappa_*) \quad (6.21)$$

and

$$c_{44}(\kappa_*) = - (2 + 2\hat{\delta} + \hat{\delta}^2 - \delta^2 \kappa_*^2) \mathcal{J}_2(\kappa_*). \quad (6.22)$$

The fixed point is stable if and only if none of the eigenvalues of the matrix in (6.19) has positive real part. However, one may easily verify that $c_{32}, c_{33}, c_{44} \geq 0$ for all κ_* and δ . Furthermore, if λ is an eigenvalue of the linear system, then λ satisfies the characteristic equation,

$$\lambda^4 + \gamma (c_{33} + c_{44}) \lambda^3 + \gamma^2 c_{33} c_{44} \lambda^2 + \gamma^2 c_{32} = 0. \quad (6.23)$$

By Decarte's Law of Signs, (6.23) has no positive real roots and either zero or two negative real roots. Let $\lambda_1, \lambda_2, \lambda_3, \lambda_4$ be the roots of (6.23). Without loss of generality, we may write $\lambda_1 = \zeta + i\eta$ and $\lambda_2 = \zeta - i\eta$ for real ζ, η and $\eta \neq 0$, since at least two

of the roots are not real. From (6.23),

$$0 = \lambda_1 \lambda_2 (\lambda_3 + \lambda_4) + (\lambda_1 + \lambda_2) \lambda_3 \lambda_4 \quad (6.24)$$

$$= (\zeta^2 + \eta^2) \operatorname{Re}(\lambda_3 + \lambda_4) + 2\zeta \lambda_3 \lambda_4. \quad (6.25)$$

Hence, if λ_3 and λ_4 are both real and negative, $\zeta > 0$, and $\operatorname{Re}\lambda_1 > 0$. Otherwise, λ_3 and λ_4 must be complex conjugates, so that ζ and $\operatorname{Re}\lambda_3 = \operatorname{Re}\lambda_4$ have opposite signs. Therefore, in either case, at least one of the eigenvalues has positive real part which implies that the fixed point of the journal bearing is unstable.

6.3 The fixed outer cylinder

We now allow the inner cylinder to rotate and translate freely; recall that the inner cylinder's motion is determined by (6.2)-(6.4).

This system has the fixed point, $(\kappa, \beta, \Omega_a) = (\kappa_*, \pi/2, \Omega_{a*})$, where

$$\Omega_{a*} = \frac{(1 + \hat{\delta})^2 \hat{\Omega}_b}{(1 + \hat{\delta})^2 - 2\hat{\delta}^2 \kappa_*^2 \hat{\Delta} \mathcal{J}_2(\kappa_*)} \quad (6.26)$$

and

$$\hat{\Omega}_b = -\frac{(1 + \hat{\delta})^2 - 2\hat{\delta}^2 \kappa_*^2 \hat{\Delta} \mathcal{J}_2(\kappa_*)}{\kappa_* (1 + \hat{\delta})^2 \mathcal{J}_1(\kappa_*) [1 + (1 + \hat{\delta})^2 - 2\hat{\delta}^2 \kappa_*^2 \hat{\Delta} \mathcal{J}_2(\kappa_*)]}. \quad (6.27)$$

In an experiment, we would control the rotation of the outer cylinder and therefore $\hat{\Omega}_b$. However, to locate the fixed point it is more expedient to fix κ_* and compute the corresponding $\hat{\Omega}_b$. The relation between κ_* and $\hat{\Omega}_b$ is illustrated in figure 6-1. Linear stability analysis reveals that the fixed point is stable over a parameter regime like that illustrated in figure 6-2. Direct numerical computations of solutions to the dynamical system confirm the predictions of this figure (see figures 6-3-6-5). The first of these figures displays an example in which the equilibrium point is unstable. The system spirals away from the fixed point, and ultimately latches onto a solution that diverges

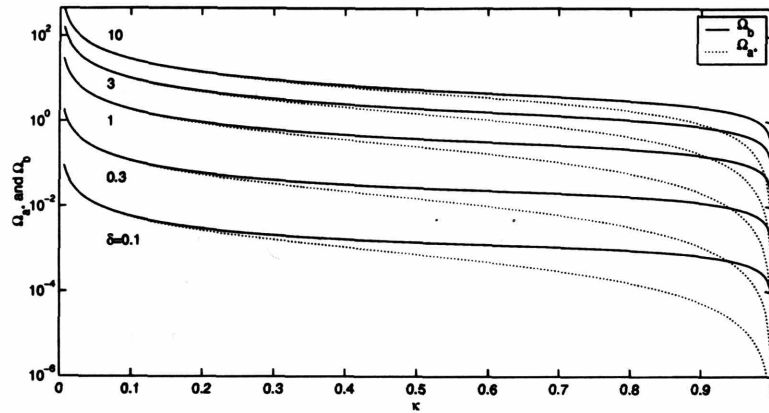


Figure 6-1: The relation between $\hat{\Omega}_b$, Ω_{a*} and κ_* for several values of $\hat{\delta} = (b - a)/a$ (as labeled).

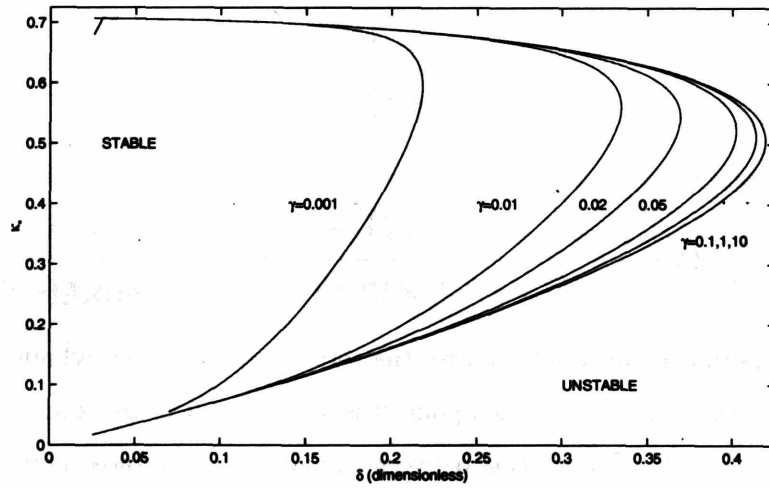


Figure 6-2: Stability boundaries of the equilibrium point on the $(\hat{\delta}, \kappa_*)$ -plane for several values of γ (as indicated). Note that γ is defined in (6.5), κ_* is defined by (6.27), and $\hat{\delta} = (b - a)/a$.

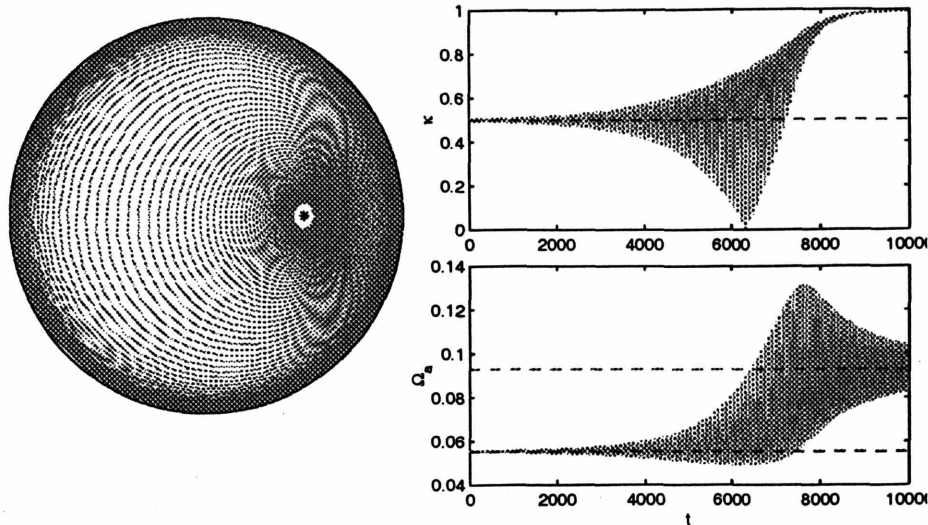


Figure 6-3: Phase portraits and time series for $\hat{\delta} = 0.5$, $\kappa_* = 0.5$ and $\gamma = 0.1$. The phase portrait shows the locus of the center of the inner cylinder on the (X_i, Z_i) -plane. The outer circle shows the limiting curve on which the inner cylinder touches the outer one, and the star shows the equilibrium point, $(\hat{\delta}\kappa_*, 0)$. The time series of $\kappa(t)$ also shows κ_* , and the horizontal lines in the plot of $\hat{\Omega}_a(t)$ show $\hat{\Omega}_b$ and $\hat{\Omega}_{a*}$.

to $\kappa = 1$, whereupon the inner cylinder touches the outer. The orbital motion of the inner cylinder then becomes locked to the outer cylinder and the rotation rate of the inner cylinder approaches $\hat{\Omega}_b$. Over much of the parameter space, it appears that the solution invariably finds such a singular solution, and so the fate of the system is for the two cylinders to come into contact. The second figure shows an example in which the equilibrium point is stable, and solutions are able to spiral into that fixed point. However, the diverging solution still exists, and the fate of the system depends on the initial conditions. The phase portrait on figure 6-4 suggests that the basins of attraction of the two solutions are bordered by an unstable limit cycle and its stable manifolds. The unstable periodic orbit can be traced back to the onset of instability of the equilibrium point on the lower branch of the stability boundary in figure 6-2, which further indicates that this transition to instability occurs via a sub-critical (Hopf) bifurcation. Figure 6-5 shows a third example which lies near the upper branch of the stability boundary. In this instance, trajectories of the solution

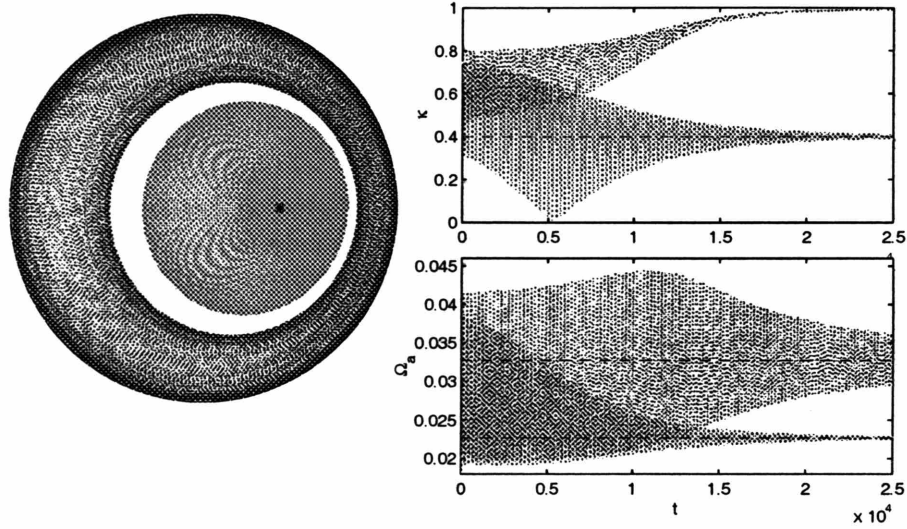


Figure 6-4: Phase portraits and time series for $\hat{\delta} = 0.3$, $\kappa_* = 0.4$ and $\gamma = 0.01$. The phase portrait shows the locus of the center of the inner cylinder on the (X_i, Z_i) -plane. The outer circle shows the limiting curve on which the inner cylinder touches the outer one, and the star shows the equilibrium point, $(\hat{\delta}\kappa_*, 0)$. Two solutions are shown; one converges to the stable equilibrium, the other diverges towards the outer cylinder. The time series of $\kappa(t)$ also shows κ_* , and the horizontal lines in the plot of $\hat{\Omega}_a(t)$ show $\hat{\Omega}_b$ and $\hat{\Omega}_{a*}$.

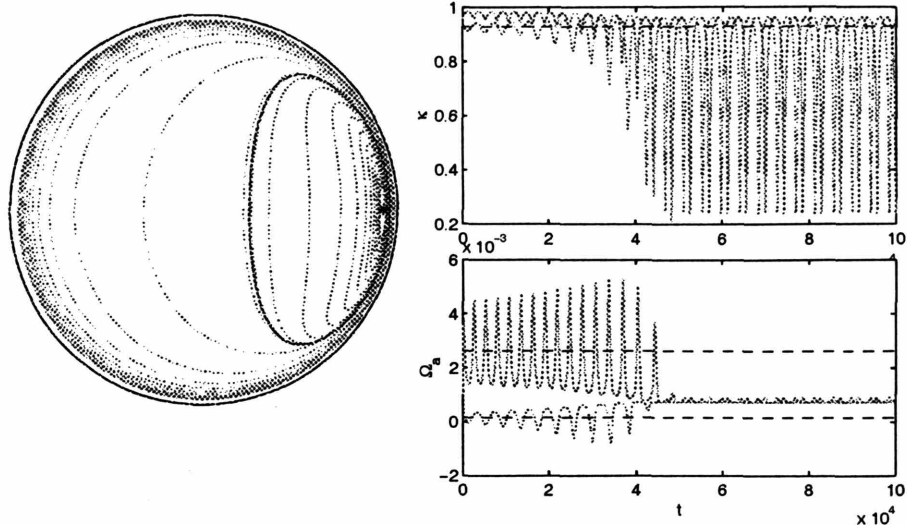


Figure 6-5: Phase portraits and time series for $\hat{\delta} = 0.176$, $\kappa_* = 0.93$ and $\gamma = 0.02$. The phase portrait shows the locus of the center of the inner cylinder on the (X_i, Z_i) -plane. The outer circle shows the limiting curve on which the inner cylinder touches the outer one, and the star shows the equilibrium point, $(\hat{\delta}\kappa_*, 0)$. Two solutions are shown, each converging to a stable limit cycle. The time series of $\kappa(t)$ also shows κ_* , and the horizontal lines in the plot of $\hat{\Omega}_a(t)$ show $\hat{\Omega}_b$ and $\hat{\Omega}_{a*}$.

approach a stable limit. That periodic orbit can also be traced back to the onset of instability along the upper branch of the stability boundary, showing that the bifurcation is supercritical along the upper branch.

6.3.1 Adding a sliding contact

Given that the inner cylinder often looks to fall onto the outer one, we are left needing to revise the theory to take into account a contact between the two cylinders. Following Smart, et al. [18], we assume that the surfaces are rough, and that when contact occurs, it does so at a small number of distinct points. The cylinders surfaces mostly remain a certain distance apart, and the lubrication gap is prescribed by this distance. *i.e.* we take κ to be given by a maximum value, $\kappa_m \equiv 1 - \delta_s/\delta$, where δ_s is the rough separation at contact, *i.e.* the average minimum gap size possible due to surface irregularities. Now, in addition to the hydrodynamic forces and gravity, a normal reaction and a sliding friction force act on the inner cylinder. Provided

that the cylinders remain in contact, the rotational and angular equations of motion become

$$\frac{1}{2}\dot{\Omega}_a = \gamma \frac{m_e}{m_a} \hat{\delta}^2 \kappa_m^2 \mathcal{J}_{1m}(\hat{\Omega}_a - \dot{\beta}) - \frac{\gamma \frac{m_e}{m_a} (1 + \hat{\delta})^2 \mathcal{J}_{1m}}{2\hat{\Delta}_m \mathcal{J}_{2m}} (\hat{\Omega}_a - \hat{\Omega}_b) - af \quad (6.28)$$

and

$$\kappa_m \ddot{\beta} = -\gamma \kappa_m \mathcal{J}_{1m} [\hat{\Omega}_a - \dot{\beta} + (1 + \hat{\delta})^2 (\hat{\Omega}_b - \dot{\beta})] - \gamma \sin \beta - f, \quad (6.29)$$

where f represents the effect of sliding friction at the rough contact, and the subscript m refers to the quantity evaluated for $\kappa = \kappa_m$. The equation of motion for κ is discarded, given that we are assuming that the normal reaction perfectly balances all other radially directed forces. If we assume further that $f \approx 0$, then we can simply avoid reformulating the equations and instead simply set $\kappa = \kappa_m$ should the integration predict values of κ beyond this limit. In this way, we may integrate the system up to rough contact, and then continue to follow the inner cylinder as it slides along the outer one. However, rough contact can also be broken if the radial motion of the inner cylinder becomes reversed and this object begins to fall away from the outer cylinder. This may arise if the inner cylinder slides all the way up to the underside of the top section of the outer cylinder. To account for this situation, we must track the radial acceleration, and restart the integration of the full system of equations should $\dot{\kappa}$ become negative. The algorithm is conveniently expressed by introducing a variable, $V(t)$, analogous to radial speed, and then writing the radial equation of motion in the form,

$$\dot{\kappa} = \begin{cases} 0 & \text{if } \kappa \geq \kappa_m \text{ and } V > 0, \\ V & \text{otherwise,} \end{cases} \quad \dot{V} = \kappa \dot{\beta}^2 + \gamma \mathcal{J}_2 (2 + 2\delta + \delta^2 - \delta^2 \kappa^2) V + \gamma \cos \beta. \quad (6.30)$$

The modified system predicts the dynamics illustrated in figure 6-6. For higher values of κ_* (lower rotation rates of the outer cylinder), the inner cylinder falls onto the lower surface of the outer cylinder, then slides partly around that surface and comes to rest

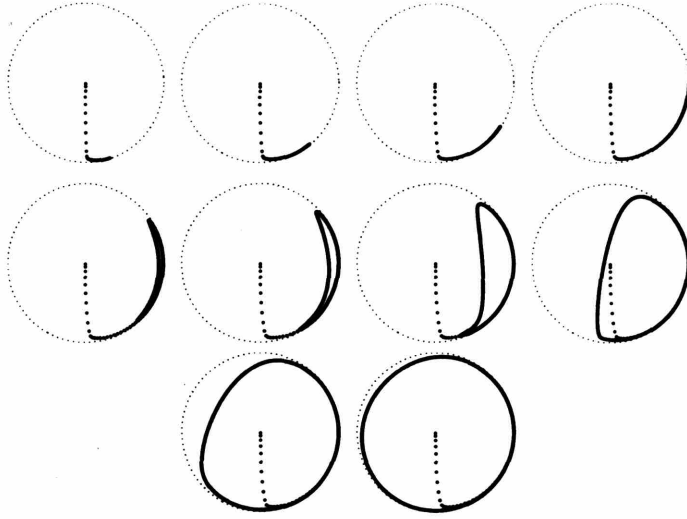


Figure 6-6: Sliding inner cylinder: Phase portraits of the locus of the center of the inner for $\hat{\delta} = 2$, $\gamma = 0.1$ and several values of κ_* (top row: 0.999, 0.996, 0.993, 0.99, middle row: 0.984, 0.983, 0.982, 0.981, bottom row: 0.98 and 0.978), which correspond to a sequence of increasing rotation rates of the outer cylinder.

at an equilibrium position (top row of the figure). The equilibrium state is given by

$$\beta = -\sin^{-1} \left\{ \kappa_m \mathcal{J}_{1m} [\hat{\Omega}_a + (1 + \hat{\delta})^2 \hat{\Omega}_b] \right\} \quad (6.31)$$

and

$$\hat{\Omega}_a = \frac{(1 + \hat{\delta})^2 \hat{\Omega}_b}{(1 + \hat{\delta})^2 - \hat{\delta}^2 \kappa_m^2 2 \hat{\Delta}_m \mathcal{J}_{2m}}. \quad (6.32)$$

Since $1 - \kappa_m \approx 0$, we see that

$$\beta \rightarrow \sin^{-1} \left[\frac{\kappa_m}{2\hat{\delta}^3} \sqrt{\frac{(1 + \hat{\delta})^5}{1 - \kappa_m^2}} \hat{\Omega}_b \right] \equiv \sin^{-1} \left[\frac{\hat{\Omega}_b}{\hat{\Omega}_{bm}} \right] \quad (6.33)$$

and

$$\hat{\Omega}_a = \frac{(1 + \hat{\delta})(1 - \kappa_m^2) \hat{\Omega}_b}{3\kappa_m^2} \approx 0. \quad (6.34)$$

As we lower κ_* (raise $\hat{\Omega}_b$), the equilibrium position of the inner cylinder lies higher and higher. Eventually, that equilibrium is lost when β exceeds $\pi/2$ and the rough contact becomes broken because the inner cylinder falls away from the outer one.

From (6.33), we see that this occurs for $\kappa_* = \kappa_m$ (the minimum separation equals the equilibrium separation without contact). Oscillations in the position of the inner cylinder then begin, first close by $\beta = \pi/2$, but of increasing amplitude as κ_* is raised still further (see the remaining rows of figure 6-6). For much lower κ_* (higher rotation rates), the inner cylinder orbits close to the outer cylinder, and near the minimum separation.

6.4 Summary

We have adapted the model of chapter 5 to incorporate the effects of surface roughness yielding a series of numerical experiments in figure 6-6 that appear to model the steady and oscillating modes observed in the experiments to be detailed in the next chapter. Furthermore, we will find that the model may be calibrated by choosing κ_m so that the model and experiment yield very similar results.

Chapter 7

Experiments

In this chapter, we compare our numerical simulations of chapter 6 with additional experiments performed with the stationary apparatus (figure 2-4). Then we performed additional experiments with the snail cylinders (figure 2-1) in order to interpret the quasi-steady rolling modes in terms of surface roughness in chapter 8.

7.1 Comparison of simulation and experiment with the fixed outer cylinder

In order to rationalize the experiment, we must interpret the physical variables in terms of the parameters used in the model. Since the experiments were performed using the same inner cylinder, we consider the dimensionless $\hat{\delta} \equiv (b-a)/a = 3.2$ to be fixed in the model. Furthermore, since the total variation of the fluid density was less than 2 percent throughout the silicon oil experiments, we take the fluid density as fixed at $\rho = .96gcm^{-3}$. This leaves only γ and κ_* as independent, dimensionless parameters in the numerical model and ν and Ω_b as independent, dimensional parameters in the lab. From (6.1), (6.5) and (6.27), we may write

$$\nu = (7.53cm^2s^{-1}) \gamma^{1/2}, \quad (7.1)$$

$$\Omega_b = - (.68s^{-1}) \left(\frac{1 - 1.16\kappa_*^2 \Delta \mathcal{J}_2(\kappa_*)}{\kappa_* \mathcal{J}_1(\kappa_*) [1 - 1.10\kappa_*^2 \Delta \mathcal{J}_2(\kappa_*)]} \right) \gamma^{-1/2}. \quad (7.2)$$

Furthermore, we may use these expressions to express standard laboratory dimensionless quantities, Reynolds and Froude numbers, in terms of the numerical parameters. We have

$$\text{Re} = \frac{\Omega_b b^2}{\nu} = -\frac{2.5}{\gamma} \left(\frac{1 - 1.16\kappa_*^2 \Delta \mathcal{J}_2(\kappa_*)}{\kappa_* \mathcal{J}_1(\kappa_*) [1 - 1.10\kappa_*^2 \Delta \mathcal{J}_2(\kappa_*)]} \right), \quad (7.3)$$

$$\text{Fr} = \frac{\Omega_b^2 b}{g} \frac{\rho_f}{\rho_a - \rho_f} = \frac{1.29 \times 10^{-3}}{\gamma} \left(\frac{1 - 1.16\kappa_*^2 \Delta \mathcal{J}_2(\kappa_*)}{\kappa_* \mathcal{J}_1(\kappa_*) [1 - 1.10\kappa_*^2 \Delta \mathcal{J}_2(\kappa_*)]} \right)^2. \quad (7.4)$$

With these calculations in hand, we may consider where in the physical parameter space we may look for stable fixed points; that is, we may choose κ_* and γ and test the numerical convergence of the corresponding fixed point if it exists. However, we find that there are no stable fixed points in the numerical space with $\hat{\delta} = 3.2$. In fact, we have found no stable points with $\hat{\delta} > .5$ and expect that one can find an upper bound on $\hat{\delta}$ for which stable fixed points exist.

Therefore, in order to compare our model with our data shown in figures (7-1) and (7-2) we must turn to the sliding contact theory presented in chapter 6. To facilitate comparison, let us rewrite the non-dimensional parameters, γ and $\hat{\Omega}_b$, used in (6.28)-(6.30) in terms of the Reynolds and Froude numbers. We may write

$$\gamma = (4.84 \times 10^3) \frac{\text{Fr}}{\text{Re}^2}, \quad (7.5)$$

$$\hat{\Omega}_b = (1.07 \times 10^2) \frac{\text{Fr}}{\text{Re}}. \quad (7.6)$$

To make an appropriate choice for κ_m , note that (6.33) implies that we expect the transition between steady and oscillating modes to occur when Ω_b is such that $\kappa_* = \kappa_m$. Therefore, we choose κ_m so that Ω_b and ν , in (7.2) and (7.1), respectively, correspond to γ and $\hat{\Omega}_b$ in (7.5) and (7.6) using the Froude and Reynolds numbers for the steady point with smallest value of Re/Fr . We find $\kappa_m = .98$.

We then chose several values of the Froude and Reynolds numbers and integrated (6.28)-(6.30). In figure 7-3, the observed behaviors are superimposed onto the experimental results from figure 7-1. For the data points based on numerical simulations, we only observed the steady, oscillating and sticking modes. We believe that the

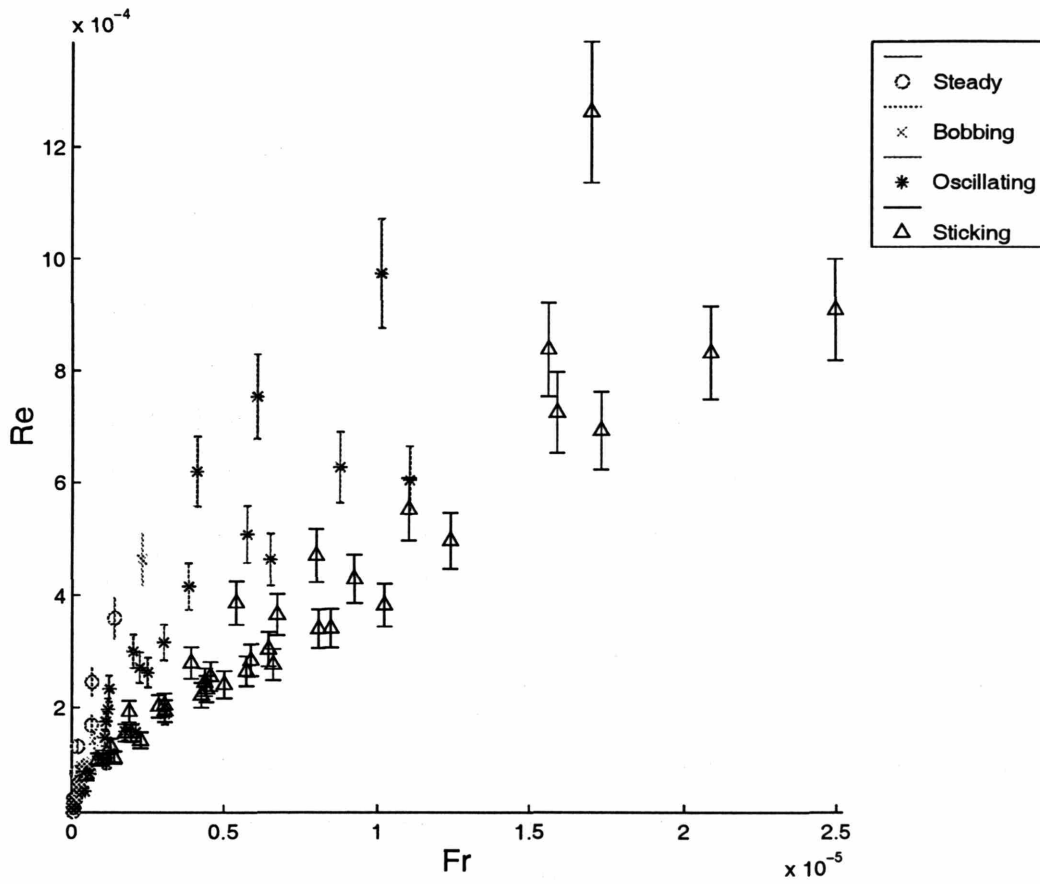


Figure 7-1: Experimental observations collected with decreasing Re . $Re \equiv \Omega_b b^2 / \nu$ is plotted against $Fr = \Omega_b^2 b / g'$, with $g' = g(\rho_a - \rho_f) / \rho_f$. Modes correspond to those defined in figure 2-5.

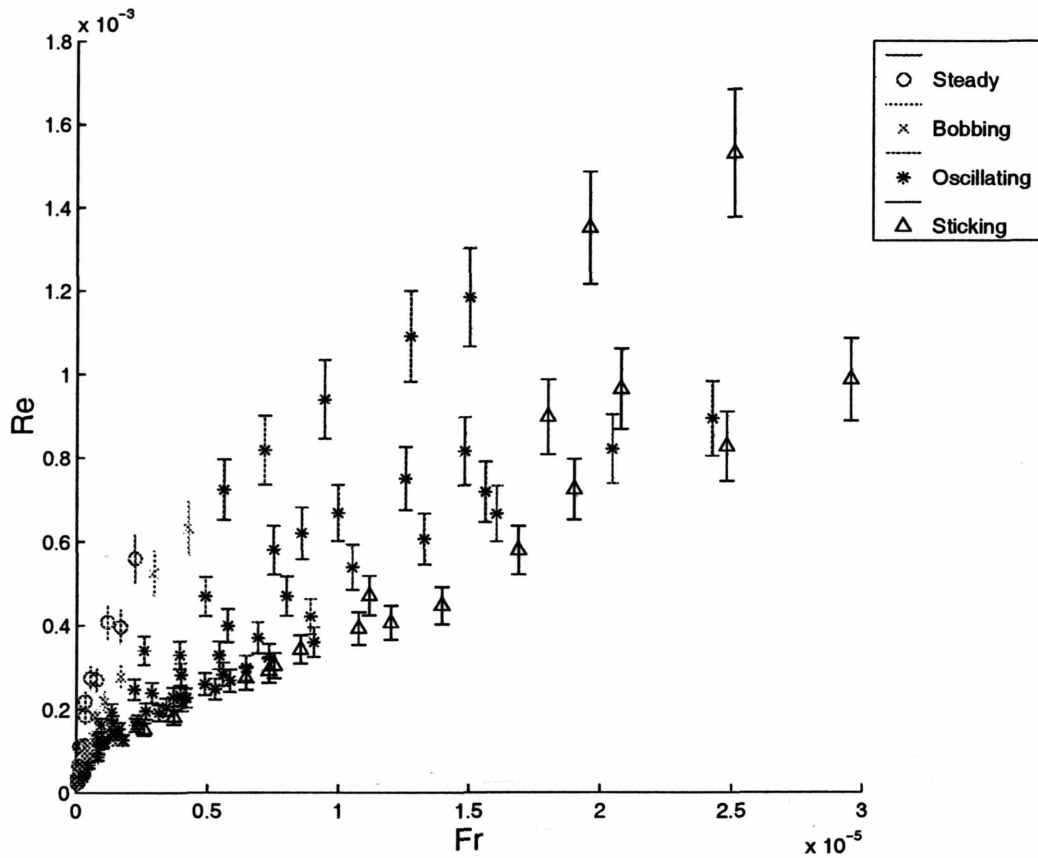


Figure 7-2: Experimental observations collected with increasing Re. $Re \equiv \Omega_b b^2 / \nu$ is plotted against $Fr = \Omega_b^2 b / g'$, with $g' = g(\rho_a - \rho_f) / \rho_f$.

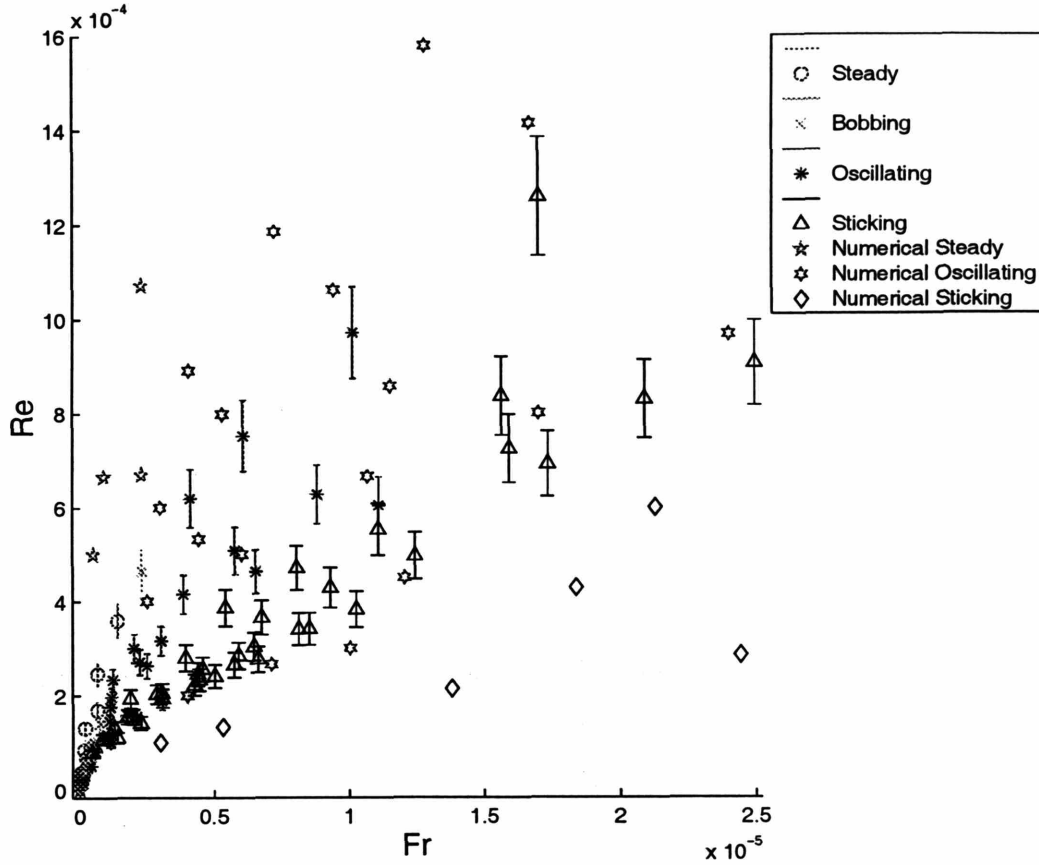


Figure 7-3: Numerically simulated results with $\kappa_m = .98$ are plotted with the observed behavior from figure 7-1. $Re \equiv \Omega_b b^2 / \nu$ is plotted against $Fr = \Omega_b^2 b / g'$, with $g' = g(\rho_a - \rho_f) / \rho_f$. The numerical points are the plus signs.

bobbing mode and the two oscillating modes that were observed are due to weak three-dimensional effects not captured by the model such as yawing and boundary effects. The numerical model predicts that transitions between modes occur at critical values of $\hat{\Omega}_b$ (represented by lines through the origin in Froude-Reynolds number space), which we recall is a ratio between the period of rotation and the settling time of the inner weight. The discrepancy between the numerics and the experiments near the sticking-oscillating transition may be due to the difficulty inherent in differentiating between the two modes visually and/or the weak three-dimensional effects.

7.2 Additional experiments with the snail cylinders

On the lowest slopes, the cylinders seem able to stop abruptly and remain completely stationary on the runway for as long as one observes them. Sometimes this resulted from the lateral drift of the inner cylinder onto one of the guiding nails piercing the bounding corks, whereupon imperfections on the edges appeared to catch the cylinder. On other occasions, the inner cylinder lay well away from the nails. Notably, when the surface of the runway was significantly smoothed (by sand-papering the surface) this residual sticking behavior was significantly reduced. Thus we concluded that the sticking was largely due to additional, uneven frictional contact between the cylinders, nail and runway, and neglected any data containing such features.

Average speeds of the outer cylinder for the various experiments are shown in figure 7-4. These averages are obtained either by linear fits to the recorded position or by taking the mean of the time required to roll 25cm during several different experiments. As illustrated in the second panel of the figure, a scaling of the speeds by the factor,

$$V_* = \frac{bM\delta g}{4\nu m_a''}, \quad (7.7)$$

looks to collapse them all down onto a single curve, where a and b denote the inner and outer cylinder radii, M is the total mass, ν is fluid viscosity, and m_a'' is the mass of fluid displaced by the inner cylinder. This scaling is predicted by theory presented below in which a rough, frictional contact is allowed between the cylinders.

Although the position of the outer cylinder on the runway was the main source of data, in one set of experiments we also measured the rotation of the inner cylinder by tracking surface markers. Figure 7-5 shows the results, plotting the dependence of average speeds, $\langle V_b \rangle = b\langle \Omega_b \rangle$ and $\langle V_a \rangle = a\langle \Omega_a \rangle$, on the runway slope, where Ω_a and Ω_b are the respective rotation rates and the angular brackets signify averages over time. For low slopes, the cylinder speeds match one another, indicating that the two cylinders roll over one another like the cogs of a gear. As the slope and speeds

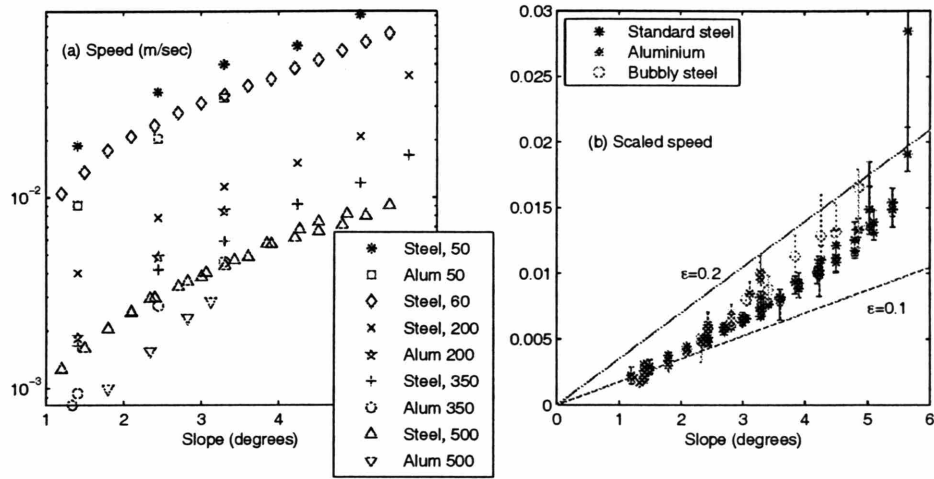


Figure 7-4: The average speeds fitted to the experiments. Panel (a) shows the raw data, plotted against slope, with the different symbols corresponding to different viscosities (as labeled in centipoise) and inner cylinders. In panel (b) we scale the speeds by the factor, V_* , in (7.7), and add rough estimates of the error bars. The two lines show theoretical predictions assuming $\epsilon = 0.1$ and 0.2 in (8.30). The data shown by green circles indicate measurements taken for 500 centiStoke oil in which a large number of small bubbles are entrained in the fluid and migrate into the narrowest part of the gap between the cylinders to form a line of cavitation.

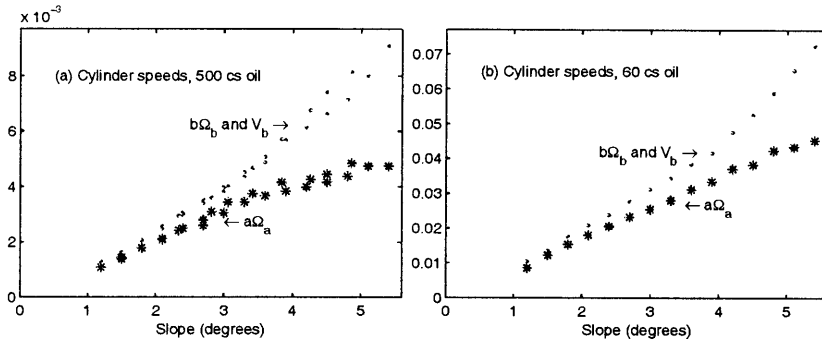


Figure 7-5: The average speeds of the two cylinders, $\langle V_a \rangle = a\langle \Omega_a \rangle$ (stars) and $\langle V_b \rangle = b\langle \Omega_b \rangle$ (dots), against slope for the steel inner cylinder and (a) 500 centiStoke and (b) 60 centiStoke oil.

increase, a sliding or reduced effective contact arises, and the inner cylinder rotates less quickly.

Theory also predicts that the speed should depend on the scale of roughness of the surfaces of the cylinders. To explore whether such a dependence is indeed present in the real cylinders, we ran experiments in which the steel cylinder was first covered with differing grades of sandpaper. The sandpapers used had scales of roughness ranging from 0.07mm to about 0.4mm (more specifically, we used 50, 80 120, 150 and 220 “grit”, American standard). The roughened cylinder speeds are compared to those of the original, smooth cylinder in figure 7-6, and are faster by an amount depending on the grade of sandpaper, confirming the dependence on roughness. In fact, the data all collapse again when we scale by a further “roughness” factor,

$$\varepsilon = \sqrt{1 - \left(1 - \frac{\sigma}{b-a}\right)^2}, \quad (7.8)$$

where σ is the actual roughness scale. The measurements suggest the roughness scales listed in table 7.1, which compare favorably with the mean particle size of the sandpapers as given by the American CAMI standard (also listed). The speed data for the smooth cylinder also collapse onto that of the roughened cylinders if it has a roughness scale of about 15 microns, which was consistent with images taken by a microscope.

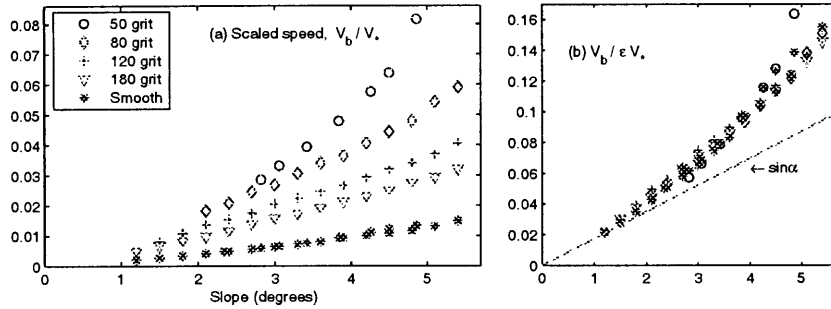


Figure 7-6: Panel (a) shows the average speeds of the outer cylinder scaled by V_* plotted against slope for the steel inner cylinder and 500 centiStoke silicone oil. The stars indicate the speeds with the usual, smooth cylinder. The circles show the speeds when the inner cylinder is covered by rough sandpaper with varying scales of roughness, as indicated. In panel (b), a further scaling of ϵ is used to collapse the data. The values used are calculated using the roughness scales listed in table 7.1.

σ (mm)	220	150	120	80	50	Smooth
Measured	0.077	0.105	0.12	0.24	0.4	0.015
Expected	0.07	0.09	0.12	0.2	0.36	

Table 7.1: Roughness scales for the various grades of sandpaper (as given by the “grit” value listed). The “measured” value indicates the number used to collapse the data in figure 7-6; the “expected” value is the number quoted by the American CAMI standard and refers to average particle size.

Note that the data for the rough cylinders begin at larger and larger inclination angles as the roughness increases because we found that the object could come to a halt on the runway if the slope was too small. This is consistent with the notion that when contact occurs between the cylinders, any roughness in the surfaces can allow inclined points of equilibrium.

We are now in the position to add the effects of surface roughness to the numerical model from chapter 4. In the next chapter, we do just that, finally reaching an understanding of the snail cylinder's quasi-steady rolling motion.

Chapter 8

Rough contact and cavitation in the rolling system

We return now to the rolling journal bearing with the insight we have gained by examining the simplified system in chapters 5 and 6. We first try to rationalize the quasi-steady rolling modes as a consequence of the cavitation bubbles observed in chapter 2. However, we find that cavitation does not generate enough force to hold the cylinders apart. Instead, we find that by adding the effect of surface roughness, we may understand the mechanism that allows the snail cylinder to roll quasi-steadily at low slopes.

8.1 Cavitation

In our experiments we observe a line of bubbles beneath the inner cylinder. If these bubbles are created by cavitation, then the air has replaced a region of very low pressure fluid. Therefore, the force on the inner cylinder will increase in the direction away from the wall so that the minimum gap thickness occurs where this increase balances the reduced weight of the inner cylinder. Upon reaching this minimum separation, we can again suppose that the system dynamics are described by the modified model (8.15)-(8.18) and use several of the conclusions reached in the previous section assuming no friction.

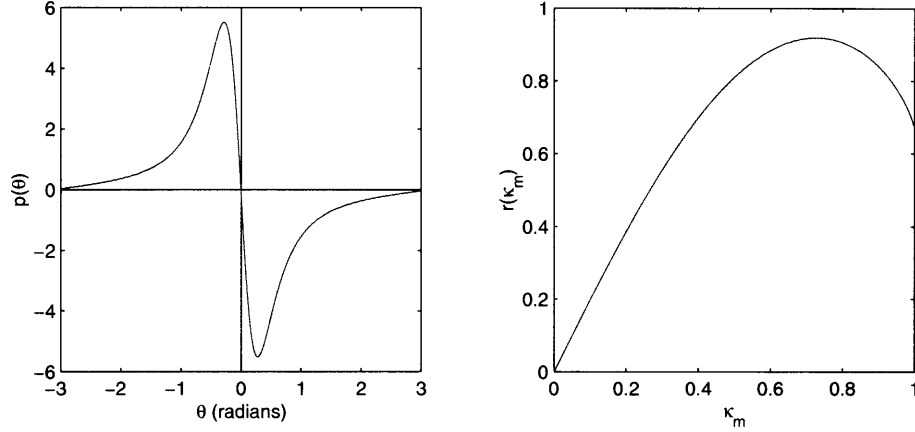


Figure 8-1: In panel (a), normalized pressure, $p(\theta)$, is plotted for $\kappa_m = 0.9$ with $(6a^2\rho\nu/\delta^2) (\Omega_a + \Omega_b - \dot{\beta}) \equiv 1$. In panel (b), r (defined in (8.13)) is plotted versus κ_m , the minimum gap size.

In section 3.3 we calculate the lubrication pressure inside the fluid gap. We quote the result from (3.32) and (3.35) for $\dot{\kappa} = 0$ (i.e. $\kappa = \kappa_m$):

$$p_\theta(\theta) = p_\theta^R(\theta) + p_\theta^S(\theta) \quad (8.1)$$

$$= \frac{12a^2\rho\nu}{(\delta - \epsilon \cos \theta)^3} (\Omega_a + \Omega_b - 2\dot{\beta}) \left[\frac{\delta - \epsilon \cos \theta}{2} - \left(\frac{1 - \kappa_m^2}{2 + \kappa_m^2} \right) \delta \right]. \quad (8.2)$$

Integrating (8.2) gives us an expression for the pressure as a function of θ . We have

$$p(\theta) = (6a^2\rho\nu/\delta^2) (\Omega_a + \Omega_b - \dot{\beta}) \kappa_m \left(\frac{-2 + \kappa_m \cos \theta}{2 + \kappa_m^2} \frac{\sin \theta}{(1 - \kappa_m \cos \theta)^2} \right), \quad (8.3)$$

which is plotted in figure 8-1(a).

We note that $p(\theta)$ has a local minimum with $\theta_0 > 0$. This minimum occurs at

$$\theta_0 = \cos^{-1} \left(\frac{\kappa_m}{2 + \kappa_m^2} \right), \quad (8.4)$$

where we expect the bubble to form. Note that as $\kappa_m \rightarrow 1$, the center of the bubble approaches the minimum separation point at $\theta = 0$. More formally, defining $\epsilon =$

$1 - \kappa_m^2$ as before, we have

$$\theta_0 \sim \sqrt{\frac{\varepsilon}{3}} \left(1 - \frac{19}{12\sqrt{3}}\varepsilon \right) + O(\varepsilon^{5/2}). \quad (8.5)$$

Near this minimum we have (recalling that $\Omega_b = 3s\varepsilon$, $\Omega_a = 0$, and $\sin \varphi = s$)

$$p(\theta) \sim -\frac{18sa^2\nu}{\tau\delta^2} \left[\frac{(1-\varepsilon)^{1/2}(3+\varepsilon)^{3/2}}{8(3-\varepsilon)}\varepsilon^{-1/2} - \frac{(1-\varepsilon)^{1/2}(3+\varepsilon)^{1/2}(3-\varepsilon)^2}{32}\varepsilon^{-3/2}(\theta-\theta_0)^2 \right]. \quad (8.6)$$

We see that as $\varepsilon \rightarrow 0$, $p(\theta_0) \rightarrow -\infty$ and that if we assume that a bubble exists for $\theta_1 = \theta_0 - \Theta < \theta < \theta_2 = \theta_0 + \Theta$, we approximate the effective increase in normal force by

$$F_N = \frac{3sa^3L\nu}{4\delta^2\tau} \left[(1-\varepsilon)^{1/2}(3+\varepsilon)^{1/2}(3-\varepsilon)^2\varepsilon^{-3/2} \right] \Theta^3. \quad (8.7)$$

If we assume that the bubble extends to the minimum separation point, then $\Theta \sim \sqrt{\varepsilon}$ and F_N is an $O(1)$ term which should be included in the force balance and could, in principle, make a significant contribution to the effect holding the inner cylinder off the outer cylinder's wall.

To compare the effect with the experimental data, we can attempt to find an appropriate cut-off pressure in order to achieve $\varepsilon \sim 0.14$ as implied by the experimental data. To that end, we note that $p(\theta)$ has a closed-form anti-derivative given by

$$\int p(\theta) a d\theta = \frac{18sa^3\rho\nu/\delta^2\tau}{(2+\kappa_m^2)} \left[\frac{1}{1-\kappa_m \cos \theta} - \log(1-\kappa_m \cos \theta) \right], \quad (8.8)$$

which simplifies calculating the restorative force given the vapor pressure where the pressure is cut-off by the bubble. If the bubble satisfies $\theta_1 \leq \theta \leq \theta_2$ where the pressure is cut-off at $p(\theta_1) = p(\theta_2)$, we can calculate the net normal force on the inner cylinder. That is

$$\begin{aligned} F_N &= \int_{\theta_1}^{\theta_2} [p(\theta_1) - p(\theta)] a L d\theta \\ &= \frac{18sa^3L\rho\nu/\delta^2\tau}{2+\kappa_m^2} \left[\kappa_m \left(\frac{(-2+\kappa_m \cos \theta_1) \sin \theta_1}{(1-\kappa_m \cos \theta_1)^2} \right) (\theta_2 - \theta_1) \right] \end{aligned} \quad (8.9)$$

$$+ \frac{\kappa_m (\cos \theta_1 - \cos \theta_2)}{(1 - \kappa \cos \theta_1)(1 - \kappa_m \cos \theta_2)} + \log \left(\frac{1 - \kappa_m \cos \theta_1}{1 - \kappa_m \cos \theta_2} \right) \Big]. \quad (8.10)$$

At a stable configuration, this normal force must cancel the effective gravitational force pushing the inner cylinder towards the wall when $\cos \varphi = s$ and $\Omega_b = 3s\varepsilon/\tau$. That is $F_N = m'_a g s$. Therefore, we wish to solve the following system of equations for the cut-off pressure, p_c . Furthermore, we seek a solution for a $\kappa_m \sim 0.14$.

$$c \equiv \frac{2aL\pi}{3sgm'_a} \frac{2 + \kappa_m^2}{\kappa_m} p_c = \frac{-2 + \kappa_m \cos \theta_1}{(1 - \kappa_m \cos \theta_1)^2} \sin \theta_1 = \frac{-2 + \kappa_m \cos \theta_2}{(1 - \kappa_m \cos \theta_2)^2} \sin \theta_2, \quad (8.11)$$

$$\frac{2\pi}{3} = \frac{1 - \kappa_m^2}{2 + \kappa_m^2} \left[\kappa_m c (\theta_2 - \theta_1) - \frac{1}{1 - \kappa_m \cos \theta_2} + \frac{1}{1 - \kappa_m \cos \theta_1} + \log \frac{1 - \kappa_m \cos \theta_2}{1 - \kappa_m \cos \theta_1} \right]. \quad (8.12)$$

Since the bubbles are relatively small, we may maximize the right hand side of (8.12) over all choices of p_c for any given κ_m by choosing $p_c = 0$. This implies $\theta_1 = 0$ and $\theta_2 = \pi$. Let us now define a function $r(\kappa_m)$ by

$$r(\kappa_m) = \frac{1 - \kappa_m^2}{2 + \kappa_m^2} \log \frac{1 + \kappa_m}{1 - \kappa_m} + \frac{2\kappa_m}{2 + \kappa_m^2}, \quad (8.13)$$

which is the right hand side of 8.12 with these choices for p_c, θ_1 and θ_2 . In figure 8-1(b), we plot $r(\kappa_m)$ as a function of κ_m and immediately see that $r < 2\pi/3$. This implies that the magnitude of the cavitation-driven restoring force, at any κ_m , will be less than that of the reduced gravity. Therefore, the effect of cavitation can, at most, be responsible for delaying the approach of the inner cylinder onto the outer cylinder. It cannot, however, account for the observed quasi-steady modes.

Ashmore, et al. [1] derive a similar set of nonlinear algebraic equations to determine the size of a bubble created by cavitation by a sphere moving next to a rotating cylinder. However, their system of equation has a solution which indicates that cavitation sets the gap size between the two bodies.

8.2 Rough contact

The theoretical solutions in chapter 4 suggest that the inner cylinder inexorably falls down onto the lower surface of the outer cylinder in the quasi-steady modes. In this circumstance, the continual thinning of the fluid gap generates a steadily increasing amount of viscous dissipation, with the result that the cylinders brake to a halt. By contrast, the cylinders in the experiment continue to roll, suggesting that the gap never really closes. One possible explanation is offered by the roughness of the cylinder surfaces: asperities on the surfaces could, in principle, prevent full contact of the cylinders and maintain a minimum gap through which fluid continues to flow. The cylinders then become free to roll steadily, but at a rate determined by the roughness of the surfaces. This is indeed what is observed experimentally. A similar argument was put forward by Smart, Beimfohr, and Leighton [18] for the motion of a sphere down an inclined plane.

Frictional contact between the two cylinders demands the inclusion of two contact forces in the equations of motion: \mathbf{C} acting on cylinder A , and $-\mathbf{C}$ on cylinder B . Thus, the equations of motion become

$$\begin{aligned}
 m_a \ddot{\mathbf{X}}_a &= \mathbf{F}_a - m_a \mathbf{g} + \mathbf{C}, \\
 m_b \ddot{\mathbf{X}}_b &= \mathbf{F}_b - m_b \mathbf{g} + \mathbf{E} - \mathbf{C}, \\
 \frac{1}{2} m_a a^2 \dot{\Omega}_a &= T_a - a C_\beta, \\
 m_b b^2 \dot{\Omega}_b &= T_b + b E_X + b C_\beta,
 \end{aligned} \tag{8.14}$$

where $\mathbf{C} = C_\epsilon \hat{\boldsymbol{\epsilon}} + C_\beta \hat{\boldsymbol{\beta}}$, with C_ϵ as the frictional component and C_β as the normal reaction. The main idea is that, when the contact is rough, \mathbf{C} prevents the cylinders from moving closer than a certain maximum distance (*i.e.* ϵ or κ), allowing fluid flow through the gap to generate finite viscous forces and torques. Thus, we set $\kappa \leq \kappa_m < 1$, where κ_m parameterizes the roughness scale.

Depending on the normal reaction, C_ϵ , the cylinder surfaces may become either locked together by the force of friction, C_β , or slide over one another when that force is less than the imposed traction. Let χ denote the effective angle of friction that

characterizes the contact between the two surfaces of the cylinders when they are immersed in oil. Then, the surfaces do not slide over one another when

$$|C_\beta| < |C_\epsilon| \tan \chi, \quad \iff b\Omega_{\mathbf{b}} = a\Omega_{\mathbf{a}}.$$

On the other hand, frictional sliding results when we violate this constraint, and then

$$C_\beta = C_\epsilon \tan \chi \operatorname{sgn}(b\Omega_{\mathbf{b}} - a\Omega_{\mathbf{a}}),$$

(assuming that the coefficients of sliding and static friction are equal).

As before, we do not deal with these equations of motion in their full glory, but make the thin-gap approximation, $\delta \ll a$, in conjunction with lubrication theory for the fluid. A key detail of the latter is that the fluid forces, f_ϵ and f_β , are order $(\delta/a)^{-1}$ larger than the torques, $T_{\mathbf{a}}$ and $T_{\mathbf{b}}$ (fluid pressure dominates shear stress in lubrication theory). Consequently, it is evident from (8.14) that the friction force, C_β , has its main effect in the rotational equation for $\Omega_{\mathbf{a}}$. On the other hand, the normal reaction, C_ϵ , is crucial in balancing the force that pushes the cylinders together. This guides us to take $\tan \chi \sim \delta/a$ (implying further that $C_\beta \sim (\delta/a)C_\epsilon$) to supplement the scalings in the reduction scheme of section 4.1. Thus, we arrive at the new system,

$$s + \kappa \sin \varphi = \mu \Upsilon \dot{\Omega}_{\mathbf{b}} + \frac{1}{2} \Upsilon \dot{\Omega}_{\mathbf{a}}, \quad (8.15)$$

$$\sin \varphi = -\frac{\kappa(\Omega_{\mathbf{a}} + \Omega_{\mathbf{b}} + 2\dot{\varphi})}{(2 + \kappa^2)(1 - \kappa^2)^{1/2}}, \quad (8.16)$$

$$\cos \varphi = \begin{cases} (1 - \kappa^2)^{-3/2} \kappa & \text{if } \kappa < \kappa_m \\ C_\epsilon & \text{if } \kappa = \kappa_m \end{cases}, \quad (8.17)$$

and

$$\frac{(1 - \kappa^2)(\Omega_{\mathbf{b}} + \dot{\varphi}) - (1 + 2\kappa^2)(\Omega_{\mathbf{a}} + \dot{\varphi})}{3(2 + \kappa^2)\sqrt{1 - \kappa^2}} = \begin{cases} \frac{1}{2} \Upsilon \dot{\Omega}_{\mathbf{a}} & \text{if } \kappa < \kappa_m \\ \frac{1}{2} \Upsilon \dot{\Omega}_{\mathbf{a}} + C_\beta & \text{if } \kappa = \kappa_m \end{cases}, \quad (8.18)$$

where

$$C_\epsilon = -\frac{C_\epsilon}{am'_a g}, \quad C_\beta = \frac{\delta C_\beta}{m'_a g}. \quad (8.19)$$

The condition that the cylinders become locked together now becomes

$$|C_\beta| < |C_\epsilon| \tan \phi, \quad (8.20)$$

where $\tan \phi = (a/\delta) \tan \chi$. But given that $\Omega_a = \Omega_b$ when this occurs, we find from (8.16) and (8.18) that

$$C_\beta = -\frac{2s + (1 - 2\mu)\kappa_m \sin \varphi}{2(1 + 2\mu)}, \quad (8.21)$$

and so locking results when

$$\left| \frac{2s + (1 - 2\mu)\kappa_m \sin \varphi}{2(1 + 2\mu)} \right| < |\cos \varphi| \tan \phi. \quad (8.22)$$

We illustrate the behavior of the model including rough contact in figure 8-2. This picture displays a solution computed from an initial condition with $\kappa(0) < \kappa_m$. The integration continues up to a “collision time”, t_m , at which point, $\kappa(t_m) = \kappa_m$. Beyond that instant, we switch to $C_\epsilon = \cos \varphi$ and continue the solution, monitoring whether or not the traction between the cylinders is sufficient to overcome friction and force the surfaces to slide over one another. In the example shown, the ultimate fate of the system is a steadily rolling solution in which the cylinders are in sliding contact. A case in which the final rolling solution has the cylinders locked together by friction is shown in figure 8-3.

Note that the computation switches abruptly between the different versions of the equations of the model. In particular, when the cylinders first come into contact, if friction is sufficient to lock the cylinders together, then Ω_a must jump discontinuously at the moment of contact. This can be rationalized physically in terms of an instantaneous impulse that affects the inner cylinder. In principle, at collision, there should also be an equal and opposite impulse acting on the outer cylinder. However, that cylinder is also resting on its contact point with the inclined plane, and the model effectively assumes that any impulse from the collision of the two cylinders is

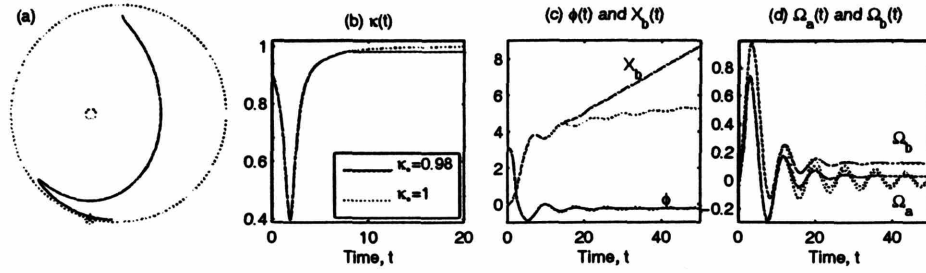


Figure 8-2: Sample rocking solution for $\Upsilon = 1$, $m_b = 0$ ($M = m_a$) and $s = 1/4$, with κ limited to the range $(0, \kappa_m = 0.98)$, and $\psi = 0.05$. The layout of panels (a)-(d) is as for figure 4-1, except that the unlimited sedimenting solution is also shown by the dotted lines.

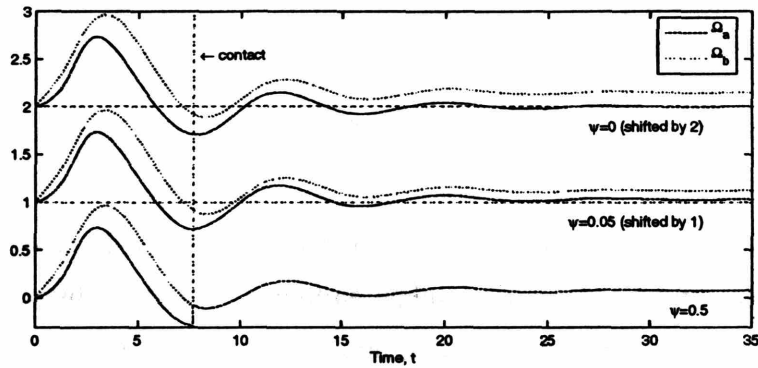


Figure 8-3: Sample solution for $\Upsilon = 1$, $m_b = 0$ ($M = m_a$) and $s = 1/4$, with $\kappa_m = 0.98$ and four values of ψ (0.5, 0.05, 0.1 and 0; the curves are offset of clarity). The vertical dashed line shows the moment of contact.

cushioned by the other contact point.

As apparent from figure 8-3, the system has a fixed point. The limiting solution is given by

$$-s = \kappa_m \sin \varphi, \quad (8.23)$$

$$\sin \varphi = -\frac{\kappa_m (\Omega_a + \Omega_b)}{(2 + \kappa_m^2)(1 - \kappa_m^2)^{1/2}}, \quad (8.24)$$

$$\cos \varphi = C_\epsilon, \quad (8.25)$$

and

$$\frac{(1 - \kappa_m^2)\Omega_b - (1 + 2\kappa_m^2)\Omega_a}{3(2 + \kappa_m^2)\sqrt{1 - \kappa_m^2}} = C_\beta. \quad (8.26)$$

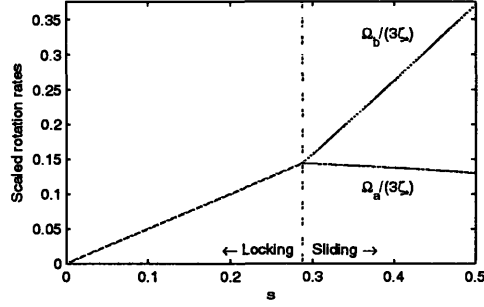


Figure 8-4: Scaled, steady rotation rates, $\Omega_a/(3\zeta_m)$ and $\Omega_b/(3\zeta_m)$, for $\phi = 0.15$.

The condition (8.22) for locking now reduces to $s < 2\sqrt{1 - s^2/\kappa_m^2} \tan \phi$, which, if true, implies that

$$\Omega_a = \Omega_b = \frac{1}{2\kappa_m^2} s(2 + \kappa_m^2) \sqrt{1 - \kappa_m^2}. \quad (8.27)$$

Otherwise,

$$\Omega_a = 3\sqrt{1 - \kappa_m^2} \cos \phi \tan \phi + \frac{s(1 - \kappa_m^2)^{3/2}}{2\kappa_m^2}, \quad \Omega_b = \frac{s(2 + \kappa_m^2)}{2\kappa_m^2} \sqrt{1 - \kappa_m^2} - \Omega_a. \quad (8.28)$$

When the minimum gap is relatively narrow, and $\zeta_m \equiv \sqrt{1 - \kappa_m^2} \ll 1$, we may write both solutions in the compact form,

$$\Omega_a = 3\zeta_* s \text{Min} \left(\frac{1}{2}, \frac{\sqrt{1 - s^2}}{s} \tan \phi \right), \quad \Omega_b = 3\zeta_* s \text{Max} \left(\frac{1}{2}, 1 - \frac{\sqrt{1 - s^2}}{s} \tan \phi \right). \quad (8.29)$$

The steady rolling speeds predicted by these formulae are illustrated in figure 8-4.

In dimensional terms, the equilibrium cylinder speed is expected to be

$$V = \frac{\epsilon b M \delta g \sin \alpha}{4\nu m_a''} \text{Max} \left(\frac{1}{2}, 1 - \frac{\sqrt{1 - s^2}}{s} \tan \phi \right). \quad (8.30)$$

The functional dependence on parameters contained in the prefactor is used to scale the experimental observations in figure 7-4. The comparison suggests that $\epsilon \sim 0.1$. In turn, this implies a roughness scale of around 15 microns, which seems reasonable in view of images taken of the surface of the cylinders with a microscope. Applying the

same approach to the rough cylinders coated with sandpaper also gives fair agreement with the expected roughness scale (based on the American CAMI standard).

The expected rotation rates (figure 8-4) also share some common points with the experimental observations (figure 7-5). For smaller slope angles, the rotation rates are closely matched, and they diverge from one another once a critical slope is exceeded. Given that the roughness of the surfaces keeps the cylinders apart and the effective minimum gap is not expected to be the same all the way around the cylinder surfaces, it is unlikely that the cylinders could ever become perfectly locked. According to the theory, the critical slope measures the friction angle for sliding; we estimate $\chi \approx 3^\circ$ given the data in figure 7-5. One notable point of disagreement is the rotation rate of the inner cylinder once sliding begins: in the theory, Ω_a decreases once sliding sets in. The observations, on the other hand, show no tendency for Ω_a to decrease.

If one were to add slight stochastic variations in κ_m , to simulate a rough angular dependence of the minimum gap size, one might imagine that the system would be randomly kicked off the equilibrium and rock slowly back to it, again similar to the observations.

In this chapter, we have completed the two-dimensional model of the snail cylinder by incorporating the dominating effect of surface roughness between the two cylinders and neglecting cavitation forces when the cylinders are very close to each other. This effect accounts for the slow quasi-steady motion which originally piqued our interest in the problem.

Chapter 9

Conclusions

We have succeeded in elucidating the subtle dynamics of the snail cylinder. To simplify the analysis, we have considered systems in which the distance between the cylinders is always small. This allows us to take advantage of the vast engineering literature on lubrication theory in general and the journal bearing in particular.

Several snail cylinders were constructed, using different inner weights and fluid viscosities, and were placed on ramps. Three distinct modes of motion were observed and recorded in chapter 2: a rocking motion, a slow, quasi-steady rolling motion, and an unbounded accelerating mode. At low inclines (i.e. less than 5 degrees), one is able to find the rocking mode, unless the cylinders are initially pushed too hard. For slopes between 1 and 5 degrees, the quasi-steady, slow rolling motion also appeared; in this case, the cylinders' velocity depends on the inner cylinder weight, fluid viscosity, and surface roughness. At higher slopes, only the unbounded, accelerating mode could be seen; in this mode, the motion appears independent of the fluid viscosity. Finally, we noted small bubbles in the system that could not be completely removed and appeared to congregate along the line of minimum separation during the slow rolling motion.

The general features of the snail cylinder dynamics can be understood by considering our theoretical model in chapters 3 and 4; these include both the observed accelerating and rocking motions. Qualitatively, we expect the system to accelerate in either of two cases: first, when its initial period of rotation is much shorter than

the settling time, i.e. $1/\Omega_b \ll \tau_s$; or second, when the gravitational component that acts on the center-of-mass of the whole system, accelerating it down the incline, dominates the effective gravitational force acting on the inner cylinder, leading it to sediment onto the outer cylinder. We note that the parameter s in the theoretical model can be rewritten as

$$s = \frac{Mg \sin \alpha}{\frac{\delta}{a} m'_a g}. \quad (9.1)$$

Therefore, our observation in chapter 4 that $s \approx 1$ allows only accelerating modes, implies that if $Mg \sin \alpha / m'_a g \gg \delta/a$, only unbounded accelerating modes are possible. Conversely, we may expect to find rocking motion if both $\tau \ll 1/\Omega_b$ and $Mg \sin \alpha / m'_a g \ll \delta/a$.

We may also distinguish between the accelerating and rocking modes by considering energy conversion within the system. The frictional force between the outer shell and the incline does no work because the contact point moves with no instantaneous velocity; therefore, any energy loss occurs within the system. In the accelerating system, the gravitational potential of the whole system is converted into kinetic energy with a minimal amount of energy dissipated into heat. Since the dissipation in the fluid is negligible, one expects and finds that the bearing's acceleration is independent of the fluid viscosity. However, in the rocking system, all potential energy is ultimately dissipated into heat by the fluid viscosity. Therefore, for the snail cylinder to roll slowly down the incline, potential energy must be dissipated in the fluid without a significant change in kinetic energy.

To understand the energetics of the snail cylinder, we studied a modified nested cylinder system in chapters 5 and 6. A cylinder was placed inside a larger fluid-filled cylinder whose angular velocity was prescribed by a motor. The discrepancy between the inner cylinder's observed motion and our predictions suggested that we include a frictional interaction between the two cylinders. By adjusting the model to account for surface roughness, we found reasonable agreement between a new series of experiments and our modified model in chapter 7.

In light of this study, we proposed that some combination of surface roughness

and cavitation holds the inner cylinder off the outer wall by supporting its weight to rationalize the quasi-steady mode. We performed more experiments in section 7.2 to test the effect of cavitation bubbles and different roughness scales on the snail cylinder's motion. Either surface roughness or cavitation could have the effect of keeping the fluid gap thickness constant at a physically determined minimum distance. In turn, a constant gap thickness would imply a constant rate of energy dissipation which is a necessary condition for slow rolling.

Following recent work by Ashmore, et al. [1], we examined the effect of cavitation bubbles underneath the inner cylinder in section 8.1. When we examine the magnitude of the resulting forces due to the bubbles, we find that cavitation is not a viable mechanism to account for the anomalous observations. That is, we find that the cavitation bubbles cannot generate enough force to hold the inner cylinder away from the outer wall. Ashmore, et al., draw a different conclusion in their work on a sphere next to the rotating cylinder wall. They predict that the minimum gap size is determined by cavitation. We reconcile these differing conclusions by noting that in the spherical problem, the pressures created in the gap are proportional to gap size to the $-3/2$; in the cylindrical problem, the pressures are only proportional to gap size to the $-1/2$, so one may expect cavitation to play a bigger roll for the sphere. Furthermore, Seddon and Mullin's observations suggest that cavitation affects the rotation of the inner cylinder; this may still be the case despite surface roughness determining the dimensions of the region where cavitation takes place.

Since cavitation cannot be the dominant effect, we build on our hierarchy of theoretical models, in section 8.2, by considering only the effect of surface roughness on the rolling speed of the quasi-steady mode, neglecting cavitation. We calculated an expected gap size that produces predicted velocities that are comparable to those seen in experiment. Furthermore, this gap size is comparable to roughness scales for the materials used to build the snail cylinders.

Summarizing, we have rationalized the curiously slow, quasi-steady rolling of the snail cylinder system. We have rephrased the problem in terms of the journal bearing so that we could take advantage of the wealth of research that has been done on that

problem. However, the standard lubrication theory explanation of the fluid dynamics within the system did not account for the particular motion that we observed. Therefore, we built upon work by Smart, et al., and Ashmore, et al., on the interaction of a sphere in Stokes flow near a moving boundary to consider the effects of surface roughness and cavitation in the cylindrical geometry. We have built these effects into the lubrication theory and have learned that dissipation in the region between the cylinders, held at a constant size by surface roughness, is the mechanism by which the cylinder's acceleration is impeded in the quasi-steady mode.

Appendix A

Dimensionless groups and physical quantities

	Definition	Section Introduced	Range of Values
μ	$\frac{M+m_b}{m_a}$	4.1	(1, 10)
Υ	$\frac{g\delta^3 m_a m_a'}{144\nu^2 m_a''^2}$	4.1	(10^{-2} , 5)
s	$\frac{a \sin \alpha M}{\delta m_a'}$	4.1	(0, 1)
γ	$\frac{64m_a''^2 \nu^2 \delta}{m_e m_a' g a^4}$	6.1	(10^2 , 10^5)
$\hat{\delta}$	$\frac{\delta}{a}$	6.1	(0, 5)
$\hat{\Omega}_b$	$\Omega_b \frac{8m_a'' \nu \delta}{m_a' g a^2}$	6.1	(0, 10)
κ_*	(6.27)	6.3	(0, 1)
Re	$\frac{\Omega_b b^2}{\nu}$	7.1	($0, 2 \times 10^{-3}$)
Fr	$\frac{\Omega_b^2 b}{g'}$	7.1	($0, 3 \times 10^{-5}$)

Table A.1: Various dimensionless groups used in the thesis

	Meaning	Notes
a	inner cylinder radius	$\in (0, 5cm)$
m_a	inner cylinder mass	$\in (.5cm, 2cm)$
L	system length	$\in (5cm, 50cm)$
b	outer cylinder radius	$\in (0, 20cm)$
m_b	outer cylinder mass	$\approx 46g$
Ω_b	angular velocity of outer cyl.	$\in (0, 2sec^{-1})$
ρ	fluid density	$\in (.85g\ cm^{-3}, 1.5g\ cm^{-3})$
ν	fluid kinematic viscosity	$\in (1cm^2\ sec^{-1}, 12000cm^2\ sec^{-1})$
m_f	fluid mass	$\pi\rho L(b^2 - a^2)$
M	total system mass	$m_a + m_b + m_f$
m_a''	displaced fluid mass	$\pi\rho a^2 L$
m_a'	m_a reduced by buoyancy	$m_a - m_a''$
τ_s	rolling time scale	$12 \frac{m_a'' \nu a}{m_a' \delta^2 g}$
τ_m	fixed outer cylinder time scale	$8 \frac{m_a'' \nu \delta}{m_a' g a^2}$

Table A.2: Various physical quantities and their meanings

Appendix B

The Calculations of Finn and Cox[8]

B.1 Rotlets and Stokeslets

Recall that the equations of motion for Stokes flow are

$$-\vec{\nabla}\Pi + \nu\nabla^2\vec{u} = 0 \tag{B.1}$$

$$\vec{\nabla} \cdot \vec{u} = 0. \tag{B.2}$$

Since the flow is two dimensional, the second equation implies that we can write

$$\vec{u} = \vec{\nabla} \wedge [\Psi(x, y, t) \hat{z}] \tag{B.3}$$

$$= \frac{\partial\Psi}{\partial y} \hat{x} - \frac{\partial\Psi}{\partial x} \hat{y}. \tag{B.4}$$

Taking the curl of the momentum equation gives

$$\nabla^2 \left[\vec{\nabla} \left(\vec{\nabla} \cdot (\Psi \hat{z}) \right) - \nabla^2 (\Psi \hat{z}) \right], \tag{B.5}$$

so that the fact that Ψ is independent of z yields

$$\nabla^4 \Psi = 0. \quad (\text{B.6})$$

Introducing the complex notation, $w = x + iy$ and $\bar{w} = x - iy$, the biharmonic equation is equivalent to the complex equation

$$\frac{\partial^4 \Psi}{\partial w^2 \partial \bar{w}^2} = 0, \quad (\text{B.7})$$

which is easily seen to have the (purely real) solution

$$\Psi(w, \bar{w}) = \bar{w}f(w) + w\bar{f}(\bar{w}) + g(w) + \bar{g}(\bar{w}), \quad (\text{B.8})$$

for arbitrary choices of the complex functions f and g . In their paper, Finn and Cox make an important realization. Supposing that Ψ takes the form of the general solution above with no singularities on the circle $|w| = a$, they constructed another stream function

$$\begin{aligned} \psi(w, \bar{w}) = & \bar{w}f(w) + w\bar{f}(\bar{w}) + g(w) + \bar{g}(\bar{w}) - z\bar{f}(a^2/w) - \bar{w}f(a^2/\bar{w}) - \bar{g}(a^2/w) - g(a^2/\bar{w}) \\ & + (a^2 - |w|^2) \left\{ \bar{f}'(a^2/w) + f'(a^2/\bar{w}) + w^{-1}\bar{g}'(a^2/z) + \bar{w}^{-1}g'(a^2/\bar{w}) \right\}. \end{aligned} \quad (\text{B.9})$$

Any singularity of Ψ at w_0 with $|w_0| < a$ will also be a singularity of ψ . ψ has additional singularities at the image points of the singularities of Ψ and perhaps at $w = 0$. Furthermore, ψ is also a solution of the biharmonic equation which generates zero velocity and has $\psi = 0$ on $|w| = a$. They then remove any nonphysical singularities at $w = 0$ of ψ by a method of successive reflections. For example, consider the stream function corresponding to a rotlet at $w = s$

$$\Psi = \frac{1}{2}C [\log(w - s) + \log(\bar{w} - s)], \quad (\text{B.10})$$

where C and s are real numbers. The corresponding ψ for the image system is

$$\psi = \bar{w}F(w) + w\bar{F}(\bar{w}) + G(w) + \bar{G}(\bar{w}), \quad (\text{B.11})$$

where

$$F(w) = \frac{Cw}{2s(w-\sigma)}, \quad G(w) = \frac{C}{2} \left\{ \log \left(-\frac{w-s}{s(w-\sigma)} \right) - \frac{\sigma}{w-\sigma} + \log w \right\}, \quad (\text{B.12})$$

where $\sigma = a^2/s$ is the image of s in $|w| = a$. We see from this expression that ψ has a new singularity asymptotic to $\log w$ at the origin. To remove this singularity, we consider a $\Psi = P \log w + P \log \bar{w}$ and find that the image of this stream function is

$$\psi = \psi = \bar{w}F_1(w) + w\bar{F}_1(\bar{w}) + G_1(w) + \bar{G}_1(\bar{w}), \quad (\text{B.13})$$

where

$$F_1 = -\bar{P}wa^{-2}, \quad G = \bar{P}(1 - \log a^2) + (P + \bar{P}) \log w. \quad (\text{B.14})$$

Therefore, if we set $P = -C/4$ and add this stream function to the image of the original rotlet stream function, we find the final stream function for the rotlet contained in a cylinder of radius a . That is

$$\psi = \frac{C}{2} \left\{ \log \frac{\sigma |w-s|^2}{s |w-\sigma|^2} + \frac{(|w|^2 - a^2)(|w|^2 - \sigma^2)}{a^2 |w-\sigma|^2} \right\}. \quad (\text{B.15})$$

A similar calculation is done for the stokeslet contained in a cylinder of radius a . After removing all non-physical singularities within the cylinder with image stokeslets, Finn and Cox calculate its stream function as

$$\begin{aligned} \psi = & \frac{1}{4} [A(w + \bar{w}) - iB(w - \bar{w})] \log \frac{\sigma |w-s|^2}{s |w-\sigma|^2} \\ & + \frac{A(|w|^2 - a^2)}{4s} \left[\frac{w+s}{w-\sigma} + \frac{\bar{w}+s}{\bar{w}-\sigma} \right] + \frac{iB(w - \bar{w})(\sigma - s)(|w|^2 - a^2)}{4s |w-\sigma|^2} \end{aligned} \quad (\text{B.16})$$

B.2 Forces and torques from the stream function

Now let us suppose that the stream function inside a circle of radius a contains a Stokes flow with stream function

$$\psi = \bar{w}F(w) + w\bar{F}(\bar{w}) + G(w) + \bar{G}(\bar{w}). \quad (\text{B.17})$$

Then since

$$\frac{\partial}{\partial x} = \frac{\partial}{\partial w} + \frac{\partial}{\partial \bar{w}}, \quad \frac{\partial}{\partial y} = i \left(\frac{\partial}{\partial w} - \frac{\partial}{\partial \bar{w}} \right), \quad (\text{B.18})$$

and $\vec{\nabla}\Pi = \nu\nabla^2 u$, we have

$$\begin{aligned} \frac{\partial \Pi}{\partial w} &= 4i\nu \frac{\partial^2}{\partial w \partial \bar{w}} \frac{\partial \psi}{\partial w} = 4i\nu F''(w), \\ \frac{\partial \Pi}{\partial \bar{w}} &= -4i\nu \frac{\partial^2}{\partial w \partial \bar{w}} \frac{\partial \psi}{\partial \bar{w}} = 4i\nu \bar{F}''(\bar{w}). \end{aligned} \quad (\text{B.19})$$

This implies that

$$\Pi = 4i\nu \left[F'(w) - \bar{F}'(\bar{w}) \right] + \Pi_o. \quad (\text{B.20})$$

We next calculate the deviatoric stress tensor. We have

$$\begin{aligned} \frac{\partial u_x}{\partial x} &= i \left(\frac{\partial}{\partial w} + \frac{\partial}{\partial \bar{w}} \right) \left(\frac{\partial \psi}{\partial w} - \frac{\partial \psi}{\partial \bar{w}} \right) \\ &= i \left(\frac{\partial^2 \psi}{\partial w^2} - \frac{\partial^2 \psi}{\partial \bar{w}^2} \right) \end{aligned} \quad (\text{B.21})$$

$$\begin{aligned} \frac{\partial u_y}{\partial y} &= -\frac{\partial u_x}{\partial x} \\ &= -i \left(\frac{\partial^2 \psi}{\partial w^2} - \frac{\partial^2 \psi}{\partial \bar{w}^2} \right) \end{aligned} \quad (\text{B.22})$$

$$\begin{aligned} \frac{\partial u_y}{\partial x} &= - \left(\frac{\partial}{\partial w} + \frac{\partial}{\partial \bar{w}} \right) \left(\frac{\partial \psi}{\partial w} + \frac{\partial \psi}{\partial \bar{w}} \right) \\ &= - \left(\frac{\partial^2 \psi}{\partial w^2} + 2 \frac{\partial^2 \psi}{\partial w \partial \bar{w}} + \frac{\partial^2 \psi}{\partial \bar{w}^2} \right) \end{aligned} \quad (\text{B.23})$$

$$\begin{aligned} \frac{\partial u_x}{\partial y} &= - \left(\frac{\partial}{\partial w} - \frac{\partial}{\partial \bar{w}} \right) \left(\frac{\partial \psi}{\partial w} - \frac{\partial \psi}{\partial \bar{w}} \right) \\ &= - \left(\frac{\partial^2 \psi}{\partial w^2} - 2 \frac{\partial^2 \psi}{\partial w \partial \bar{w}} + \frac{\partial^2 \psi}{\partial \bar{w}^2} \right) \end{aligned} \quad (\text{B.24})$$

Therefore,

$$T = 2\rho\nu \begin{pmatrix} i \left(\frac{\partial^2 \psi}{\partial w^2} - \frac{\partial^2 \psi}{\partial \bar{w}^2} \right) & - \left(\frac{\partial^2 \psi}{\partial w^2} + \frac{\partial^2 \psi}{\partial \bar{w}^2} \right) \\ - \left(\frac{\partial^2 \psi}{\partial w^2} + \frac{\partial^2 \psi}{\partial \bar{w}^2} \right) & -i \left(\frac{\partial^2 \psi}{\partial w^2} - \frac{\partial^2 \psi}{\partial \bar{w}^2} \right) \end{pmatrix}. \quad (\text{B.25})$$

Since both Π and T are real, we can use complex notation to calculate the force on the outer cylinder due to the fluid. That is we can write $\hat{n} = w/a$, so that

$$\begin{aligned} \mathbf{F} &= \int_{|w|=a} (\rho\Pi\hat{n} - T \cdot \hat{n}) dl \\ &= 4\rho\nu i \int_0^{2\pi} \left[wF'(w) - w\bar{F}'(\bar{w}) + \bar{w} \frac{\partial^2 \psi}{\partial \bar{w}^2} \right] d\theta \\ &= 4\rho\nu i \int_0^{2\pi} \left[wF'(w) - w\bar{F}'(\bar{w}) + a^2\bar{F}''(\bar{w}) + \bar{w}\bar{G}''(\bar{w}) \right] d\theta \\ &= 4\rho\nu \int_{|w|=a} \frac{d}{dw} F(w) dw - 4\rho\nu \int_{|w|=a} \frac{d}{d\bar{w}} \left[\frac{a^2}{\bar{w}} \bar{F}'(\bar{w}) + \bar{G}'(\bar{w}) \right] d\bar{w} \\ &= -4\rho\nu \left\{ -F(w) + w\bar{F}'(\bar{w}) + \bar{G}'(\bar{w}) \right\}_C, \end{aligned} \quad (\text{B.26})$$

where $\{H\}_C$ is the change in the value of H when we go around the C one time in the counter-clockwise direction. We can also calculate the moment generated by the fluid motion on the outer cylinder using complex methods. We have

$$T_o = \int_{|w|=a} \vec{r} \wedge (\rho\Pi - T \cdot \hat{n}) dl \quad (\text{B.27})$$

$$= -Im \left\{ 4\rho\nu i \int_0^{2\pi} \bar{w} \left[wF'(w) - w\bar{F}'(\bar{w}) + \bar{w} \frac{\partial^2 \psi}{\partial \bar{w}^2} \right] d\theta \right\} \quad (\text{B.28})$$

$$= Im \left\{ -4\rho\nu \int_0^{2\pi} \left[a^2\bar{F}''(\bar{w}) + \bar{G}''(\bar{w}) \right] i\bar{w} d\theta \right\} \quad (\text{B.29})$$

$$= 4\rho\nu Im \left\{ \int_{|w|=a} \frac{\partial}{\partial \bar{w}} \left[a^2\bar{F}'(\bar{w}) + \bar{w}\bar{G}'(\bar{w}) - \bar{G}(\bar{w}) \right] d\bar{w} \right\} \quad (\text{B.30})$$

$$= 4\rho\nu Im \left\{ a^2\bar{F}'(\bar{w}) + \bar{w}\bar{G}'(\bar{w}) - \bar{G}(\bar{w}) \right\}_C. \quad (\text{B.31})$$

From these simplified expressions, Finn and Cox calculate the instantaneous forces and torques by choosing appropriately placed rotlets and stokeslets to satisfy the velocity boundary conditions at the boundaries of both cylinders and plugging this stream function into (B.26) and (B.31). The results are quoted above in chapter 5.

Bibliography

- [1] J. Ashmore, C. del Pino, and T. Mullin. Cavitation in a lubrication flow between a moving sphere and a boundary. *Phys. Rev. Lett.*, 94:124501, 2005.
- [2] B. Y. Ballal and R. S. Rivlin. Flow of a newtonian fluid between eccentric rotating cylinders: Inertial effects. *Arch. Rat. Mech. Anal.*, 62(3):237–294, 1976.
- [3] N. J. Balmforth, D. P. Vener, J. W. M. Bush, and W. R. Young. A numerical and experimental investigation of the cylindrical mixer. *J. Fluid Mech.* (in preparation), 2006.
- [4] N. J. Balmforth, D. P. Vener, J. W. M. Bush, and W. R. Young. Rocking and rolling down an incline. *J. Fluid Mech.* (in preparation), 2006.
- [5] G. K. Batchelor. *An Introduction to Fluid Dynamics*. Cambridge University Press, second edition, 1967.
- [6] J. Brindley, M. D. Savage, and C. M. Taylor. The non linear dynamics of journal bearings. *Phil. Trans. R. Soc. Lond. A*, 332:107–119, 1990.
- [7] Duffing. *Z. angew. Math. Mech. (ZAMM)*, 4:279–314, 1924.
- [8] M. D. Finn and S. M. Cox. Stokes flow in a mixer with changing geometry. *J. Eng. Math.*, 41:75–99, 2001.
- [9] A. Goldman, R. Cox, and H. Brenner. Slow viscous motion of a sphere parallel to a plane wall—i: Couette flow. *Chem. Eng. Sci.*, 22:637–651, 1967.

- [10] G. B. Jeffrey. The rotation of two circular cylinders in a viscous fluid. *Phil. Trans. R. Soc. Lond. A*, 101:169–174, 1922.
- [11] T. Mullin, Y. Li, C. del Pino, and J. Ashmore. An experimental study of fixed points and chaos in the motion of spheres in a stokes flow. *IMA Journal of Applied Mathematics*, 70:666–676, 2005.
- [12] I. A. Nyrkova, A. N. Semenov, A. R. Khokhlov, K. Linliu, and B. Chu. Motion of a probe ball in the fluid under centrifugal acceleration. *J. Phys. II France*, 7:1709–1728, 1997.
- [13] O. Pinkus and B. Sternlicht. *Theory of Hydrodynamic Lubrication*. McGraw-Hill, first edition, 1961.
- [14] A. Prokunin. On a paradox in the motion of a rigid particle along a wall in a fluid. *Fluid Dyn.*, 38:443–457, 2003.
- [15] H. Reisner. *Z. angew. Math. Mech. (ZAMM)*, 15:81–87, 1935.
- [16] O. Reynolds. On the theory of lubrication. *Phil. Trans. R. Soc. Lond.*, 177(I):157–234, 1886.
- [17] J. R. T. Seddon and T. Mullin. Reverse rotation of a cylinder in a stokes flow. *Phys. Rev Lett.* (submitted), 2006.
- [18] J. R. Smart, S. Beimfohr, and D. T. Leighton Jr. Measurement of the translational and rotational velocities of a noncolloidal sphere rolling down a smooth inclined plane at low reynolds number. *Phys. Fluids A*, 5:13–24, 1993.
- [19] A. C. Stevenson. Plane stress and plane strain in bipolar coordinates. *Phil. R. Soc. Lond.*, A184:129–179, 1945.
- [20] G. H. Wannier. A contribution to the hydrodynamics of lubrication. *Quart. Appl. Math.*, 8:1–32, 1950.
- [21] Q. Yue. *The motion of a rod in a rotating Stokes flow*. PhD thesis, Pennsylvania State University, 1995.

[22] N. E. Zhukowski. *Comm. Math. Soc. Kharkov*, 17:31–46, 1887.